Generation and propagation of cyclotron maser emissions in the finite auroral kilometric radiation source cavity

P. L. Pritchett,[1] R. J. Strangeway,[2] R. E. Ergun,[3] and C. W. Carlson[4]

Received 22 March 2002; revised 24 April 2002; accepted 2 May 2002; published 12 December 2002.

[1] The properties of the electron-cyclotron maser radiation produced in the auroral kilometric radiation (AKR) source cavity are investigated by means of two-dimensional particle-in-cell simulations and observations made by the Fast Auroral SnapshoT (FAST) Explorer. The simulations assume a population of primary auroral electrons with a downgoing shell distribution. Driven simulations in a meridional plane with a finite magnetic field gradient demonstrate that the maser radiation builds up very rapidly with decreasing altitude and that bursts of radiation with timescales of the order of 0.5 ms are produced at only 5–6 km below the injection level. Initial value simulations in a longitudinal plane show that the radiation component striking the cavity boundary at normal incidence is damped away via particle absorption and conversion to the Z mode. In contrast, the longitudinally propagating component is able to be amplified along an extended path length. The FAST observations of the electric field in the source region reveal that the polarization in the plane perpendicular to the ambient magnetic field varies between being approximately isotropic to having a substantial (as much as a factor of 100) enhancement of the ''along-track'' polarization. No evidence is found that the ''across-track'' polarization is ever dominant, and thus the AKR emissions do not form a standing wave structure between the cavity boundaries. *INDEX TERMS:* 2471 Ionosphere: Plasma waves and instabilities; 2483 Ionosphere: Wave/particle interactions; 2704 Magnetospheric Physics: Auroral phenomena (2407); 7843 Space Plasma Physics: Numerical simulation studies; *KEYWORDS:* wave-particle interaction, cyclotron maser instability, mode conversion, auroral density cavity, horseshoe electron distribution

Citation: Pritchett, P. L., R. J. Strangeway, R. E. Ergun, and C. W. Carlson, Generation and propagation of cyclotron maser emissions in the finite auroral kilometric radiation source cavity, *J. Geophys. Res.*, *107*(A12), 1437, doi:10.1029/2002JA009403, 2002.

1. Introduction

[2] The electron-cyclotron maser instability [*Wu and Lee*, 1979] is believed to be the fundamental process producing the auroral radio emissions that have been observed at all of the magnetized planets: Earth, Jupiter, Saturn, Uranus, and Neptune [e.g., *Zarka*, 1998]. In addition, the basic cyclotron maser mechanism is presumed to produce microwave spike bursts during solar flares [e.g., *Melrose and Dulk*, 1982; *Sharma et al.*, 1982] and related bursts from flare stars and close binaries [e.g., *Gary et al.*, 1982]. The terrestrial version of these radio emissions, known as auroral kilometric radiation (AKR) in view of its characteristic wavelength, offers a unique opportunity to test all aspects of the cyclotron maser process as a result of the detailed in situ observations acquired by many satellites.

[3] As articulated by *Wu and Lee* [1979], the cyclotron maser mechanism provides the following characteristic predictions: (1) emission occurs near the local electron cyclotron frequency Ω_e; (2) the plasma frequency ω_{pe} in the source region must be much smaller than Ω_e; (3) generation of the radiation occurs primarily in the right-hand extraordinary (R-X) mode. There is now strong evidence supporting all of these features. In particular, the source region for AKR is associated with a deep density cavity at high altitudes on auroral zone field lines [*Calvert*, 1981]. Despite these successes of the maser mechanism, there have remained several significant gaps in our understanding of how the maser process operates as a global mechanism in the auroral region and uncertainties as to whether it can provide a quantitative description of the AKR observations. These issues include (1) the identification of the precise free-energy source that drives the maser instability, (2) doubts that sufficient amplification could be produced within the source cavity to explain the observed intensity of AKR, (3) the origin of the fine structure appearing in the AKR spectrum at frequencies below 1 kHz, and (4) identification of the mechanism by which the AKR radiation escapes from the source cavity.

[1]Department of Physics and Astronomy, University of California, Los Angeles, California, USA.
[2]Institute of Geophysics and Planetary Physics, University of California, Los Angeles, California, USA.
[3]Department of Astrophysical and Planetary Sciences and Laboratory for Atmospheric and Space Physics, University of Colorado, Boulder, Colorado, USA.
[4]Space Sciences Laboratory, University of California, Berkeley, California, USA.

0148-0227/02/2002JA009403$09.00

[4] The identification of the free-energy source appears to have been settled by recent high-resolution electromagnetic field and 3-D electron observations made by the Fast Auroral SnapshoT Explorer (FAST) [*Delory et al.*, 1998; *Ergun et al.*, 1998; *Strangeway et al.*, 1998; *Pritchett et al.*, 1999; *Ergun et al.*, 2000; *Strangeway et al.*, 2001]. The electron distributions show clear evidence for a "horseshoe" or "shell" structure extending in a nearly circular arc from near 0° pitch angle on the downgoing side through 90° pitch angle and into the upgoing part of the distribution. These features are consistent with those expected from the combined effects of parallel electric field acceleration and magnetic mirroring of primary auroral electrons [*Chiu and Schulz*, 1978; *Pritchett and Strangeway*, 1985; *Winglee and Pritchett*, 1986]. Such a distribution is ideally suited to satisfy the cyclotron resonance condition with wave emission perpendicular to the magnetic field ($k_{\|} = 0$), and 2-D particle-in-cell (PIC) simulations [*Pritchett et al.*, 1999] show that such distributions can produce wave electric fields on the order of 500 mV/m, consistent with the FAST observations. In contrast, a loss cone distribution produces much weaker fields and requires a significant value of $k_{\|}$, corresponding to emission at angles $\smile 10°$ away from perpendicular; the observations indicate perpendicular emission to within a few degrees [*Ergun et al.*, 1998].

[5] Early estimates made by *Omidi and Gurnett* [1984] using S3-3 electron distributions showed that the observed $\partial f/\partial v_{\perp} > 0$ features were not sufficient to permit amplification of cosmic noise background to the observed AKR intensities via the maser instability. The importance of the magnetic field inhomogeneity in limiting the parallel distance over which the resonance condition can be maintained ($\sharp 20$ km) and thereby limiting the possible amplification was stressed by *Le Quéau et al.* [1985]. Both of these treatments omitted the relativistic wave dispersion corrections [*Tsai et al.*, 1981; *Wu et al.*, 1981; *Wong et al.*, 1982; *Winglee*, 1983; *Pritchett*, 1984; *Le Quéau et al.*, 1984; *Strangeway*, 1985] which are significant within the auroral cavity (where $\omega_{pe}/\Omega_e < v/c$ for the primary auroral electrons) and allow emission at 90°. This perpendicular emission permits a longer path length over which the resonance condition can be maintained and thus greater amplification. Ray-tracing calculations including this effect suggested that sufficient amplification could be obtained within a transverse path length of about 100 km [*Pritchett and Winglee*, 1989]. The observed cavity dimensions are sometimes but not always this large [*Roux et al.*, 1993; *Louarn and Le Quéau*, 1996a; *Ergun et al.*, 1998]. An alternative mechanism for increasing maser amplification was proposed by *Calvert* [1982, 1987]. He suggested that partial wave reflection at density changes within the auroral cavity could produce a true radio laser whereby the enhanced amplification resulting from multiple passes across the cavity would more than compensate for the losses out the ends. The result would be the excitation of coherent oscillations and production of a series of extremely narrow bandwidths resulting from the growth to saturation and subsequent quenching of all but a single frequency. *Louarn and Le Quéau* [1996b], guided by Viking observations of small scale cavities within the AKR source region [*Hilgers et al.*, 1992], argued that AKR is produced in thin regions with transverse widths of only a few kilometers. The amplification is then achieved via propagation in the longitudinal direction, which is tangential to the source boundaries. Since the source dimension in the longitudinal direction is typically on the order of 1000 km or more, there should be no difficulty in achieving the necessary amplification in this preferential direction.

[6] A characteristic feature of AKR is the fine structure [*Gurnett et al.*, 1979]. In high-resolution spectra obtained outside of the source region, AKR is observed to consist of many closely spaced, narrowband ($\sim$1 kHz) components that display a high degree of variability with time, sometimes rising, sometimes falling, and sometimes showing quite convoluted behavior [*Gurnett and Anderson*, 1981]. Furthermore, the bandwidth of these tones is quite variable, with values as low as 5 Hz having been inferred [*Baumback and Calvert*, 1987]. Frequency spectra obtained by FAST in the source region indicate bandwidths generally below 1 kHz and as low as 100 Hz [*Ergun et al.*, 1998]. Examination of the waveforms in the source region reveals "packet-like" structures occurring at all time resolutions down to a few ms [*Strangeway et al.*, 2001]. This would imply a "bandwidth" of a few hundred Hertz ($\Delta\omega/\Omega_e \sharp 10^{-3}$). Estimates of the bandwidth produced by the maser instability in a uniform system for a model auroral zone electron distribution are in the range $\Delta\omega/\Omega_e = 1-2 \times 10^{-3}$ [*Yoon and Weatherwax*, 1998; *Pritchett et al.*, 1999; *Bingham and Cairns*, 2000]. It remains unclear, however, what causes emissions in the source region at one altitude as opposed to a nearby one. Recent conjectures by *Pottelette et al.* [2001] suggest that the fine structure is related to elementary radiation events produced by electron holes which result from the nonlinear evolution of electron acoustic waves excited by the temperature difference between the dilute, cool electron background present at the edge of the auroral cavity and the few keV, downward drifting, primary auroral electrons.

[7] Due to the relativistic wave dispersion correction, the maser emissions extend below the R-X mode cutoff at $\omega \approx \Omega_e\,[1 + \omega_{pe}^2/\Omega_e^2]$, below Ω_e, and reaching down to the relativistic gyrofrequency Ω_e/γ. Viking [*de Feraudy et al.*, 1988] and FAST [*Ergun et al.*, 1998] observations have confirmed that the AKR spectrum extends below the local Ω_e. Since observations of AKR remote from the source region indicate that it propagates primarily in the R-X mode, it is not immediately clear how the radiation escapes from inside the cavity. A 1-D simulation model in which the radiation could propagate only perpendicular to the magnetic field indicated that there was an efficient mode conversion to the *Z* mode at a sharp density gradient separating a region of dense, cool plasma from the source cavity [*Pritchett*, 1986b]. Since the Z mode represents a trapped mode, this converted radiation would not normally be able to escape and be detected by high-altitude satellites. *Louarn and Le Quéau* [1996b] argued that the longitudinally propagating maser radiation would be able to escape from the cavity once it had reached a higher altitude (due to upward diffraction in the inhomogeneous magnetic field) where the wave frequency was above the local R-X mode cutoff. In that weaker field region the maser radiation could connect to the external free-space mode.

[8] In the present paper we address a number of these issues regarding the generation and propagation of maser radiation within a finite source cavity. The primary tools are

a pair of 2-D PIC simulation models (section 2). In both cases the initial electron distribution is taken to have a downgoing shell structure. In the meridional plane model (section 3), this electron distribution is continually injected at the high-altitude simulation boundary. The radiation builds up very rapidly with decreasing altitude, and bursts of radiation with timescales of the order of 0.5 ms are produced at only 5–6 km below the injection level. In the longitudinal plane model, initial value simulations are used to study the propagation of the maser radiation perpendicular to the magnetic field. A 1-D version of this latter model is used (section 4) to study the mode conversion process at the edge of the source cavity. The 2-D version (section 5) is used to show that at later times (which in the simulations is a proxy for propagation to higher altitude) the radiation is increasingly dominated by the component propagating in the longitudinal direction; the component propagating normal to the cavity is damped away via particle absorption and conversion to the Z mode. Section 6 uses FAST observations of all three electric field components to determine that the field polarization in the source region is either isotropic in the plane perpendicular to **B** or has an enhancement of the component with polarization normal to the cavity interface ("along-track" polarization). There is no evidence for a standing wave structure for AKR. Section 7 contains the summary and discussion.

2. Simulation Models

[9] The simplest particle simulation models that have been used to investigate the generation of AKR via the electron cyclotron maser instability employed a strictly homogeneous model in which the magnetic field and plasma density were assumed to be spatially uniform and periodic boundary conditions were employed for the fields and particles [*Pritchett and Strangeway*, 1985; *Pritchett et al.*, 1999]. Furthermore, these simulations were of the initial value type in which there was no source to replenish the electron free energy. This model was generalized by *Pritchett* [1986b] to include the effects of a finite geometry perpendicular to the ambient magnetic field. An explicit density profile was included for the auroral cavity region, and the radiation was allowed to escape from the source region along directions perpendicular to the magnetic field. The assumption of uniformity along the field lines was removed by *Pritchett and Winglee* [1989]. They incorporated a continual flow of energetic electrons through the source region and included the effects of a magnetic field gradient.

[10] In the present work we employ a modification of the driven model of *Pritchett and Winglee* [1989]. The model is illustrated schematically in Figure 1b. The simulation plane is a meridional (x,z) plane where the magnetic field $\mathbf{B}_0$ is directed in the negative z direction. The time advancement of Maxwell's equations is performed in Fourier space [*Dawson*, 1983; *Pritchett*, 1985], and the relativistic equation of motion is used for the electrons. The ions are immobile, thus forming a charge neutralizing background. A continual inflow of downgoing primary electrons ($v_{\|} > 0$) is introduced at the upper (high altitude) boundary. The velocity distribution $f(v_{\|}, v_{\perp})$ for these electrons consists of a half shell with a finite thermal spread. As the electrons travel downward, radiation is produced via the maser instability, and the radiation is removed from the system in absorbing regions at the sides and bottom of the simulation domain. Unlike the model of *Pritchett and Winglee* [1989], a constant flux condition is not imposed on the electrons. As a consequence, the number of electrons in the system can fluctuate due to small differences in the input and exit rates. Initially, the unstable shell distribution is loaded throughout the simulation domain. There is then an initial transient stage in which radiation is produced throughout the box; at later times the true driven configuration is achieved where the radiation builds up as the electrons travel downward from the high-altitude end of the system.

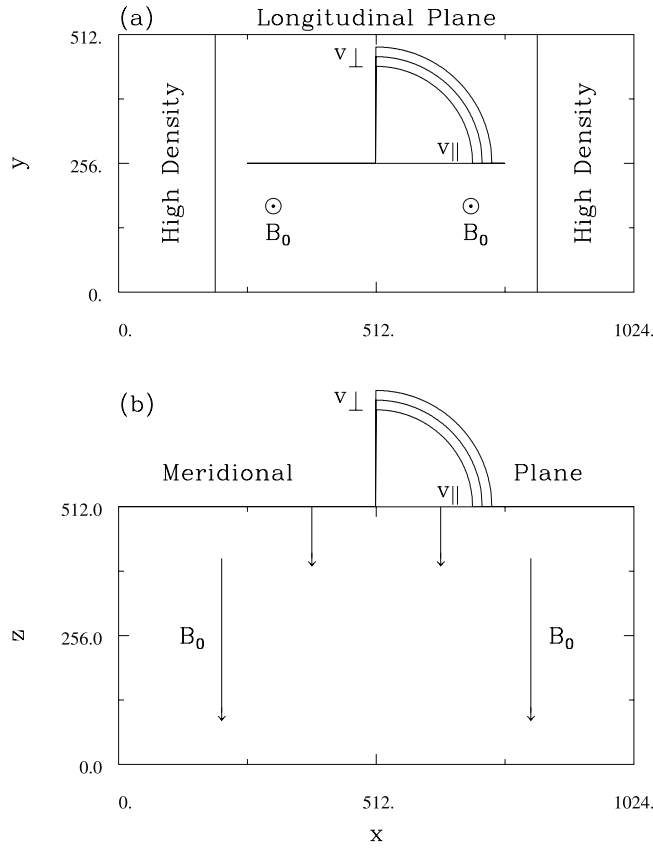

Figure 1. Two-dimensional simulation models for cyclotron maser radiation generation in the auroral cavity region. (a) Initial value model in a longitudinal (x,y) plane. Electrons with a downgoing shell distribution ($v_{\|} > 0$) are initialized throughout the central cavity; the cavity is bounded on both sides by high-density regions of thermal plasma. The ambient magnetic field is normal to the simulation plane. (b) Driven model in a meridional (x,z) plane. Electrons with a downgoing shell distribution ($v_{\|} > 0$) are continually injected into the simulation domain at the high-altitude boundary; they are removed from the system when they reach the low-altitude boundary. The magnetic field is directed downward and increases slightly in magnitude with decreasing altitude.

[11] The simulation parameters are chosen so that the maser radiation has a wavelength of 8.8Δ, where Δ is the grid spacing. For the cyclotron frequency f_{ce} = 400 kHz

typical for the FAST observations, this wavelength is 750 m, and so $\Delta = 85$ m. The simulation box size is typically $L_x \times L_z = 1024\Delta \times 512\Delta$, corresponding to 88 km across the field by 44 km along the field. (In one run the z dimension is increased to $1024\Delta = 88$ km.) For a dipole field, the magnetic gradient scale length is approximately $r/3$, where r is the geocentric altitude ($\sim 10^4$ km for FAST). Since the vertical size of the simulation box is so small, the effects of curvature of the field lines on the maser instability should be much less important than the gradient in the field strength [*Le Quéau et al.*, 1985]. Thus we adopt a straight line model in which the magnetic field has only a z component with a small gradient $(\Delta/B)dB/dz = 2.4 \times 10^{-5}$ in magnitude. In the presence of this magnetic gradient, the parallel velocity of the electrons will decrease as they stream to lower altitudes. The strength of the parallel electric field needed to counteract this decrease is $E_0 = mv_\perp^2/eL_B \approx 3$ mV/m, where L_B is the magnetic gradient scale length; this field is directed to higher altitudes. In the simulations a fluctuating E_0 is applied in order to keep the average parallel drift approximately constant in time; this field ranges between 3–10 times larger than the above estimate and has the opposite direction.

[12] Satellite observations indicate that the density of primary electrons in the AKR cavity is typically somewhat less than 1 cm^{-3} [*Perraut et al.*, 1990; *Hilgers et al.*, 1992; *Strangeway et al.*, 1998]. We thus choose a representative value of $\Omega_e/\omega_{pe} = 40$ for the simulations. The energy $mv_0^2/2$ of the shell distribution is varied between 2 and 10 keV, and the thermal spread $v_{Te}/c \approx 0.02$. The number of energetic electrons is typically about 6.1 million, and the size of the absorbing regions at the sides and bottom is 60Δ. The integration time step is $\Omega_e\Delta t = 0.2$ or equivalently $c\Delta t/\Delta x = 0.28$. A typical run covers a time interval of $\Omega_e t \approx 10^4$, which corresponds to about 4 ms.

[13] As we shall see, the maser radiation produced in the driven simulations is confined to a very small altitude range and propagates mainly perpendicular to the magnetic field. It is thus reasonable to consider an alternative model where the simulation plane is taken to be a longitudinal (x,y) plane at a constant altitude (Figure 1a). Here the magnetic field is oriented perpendicular to the simulation plane, and the simulations are of the initial value type where the shell distribution is loaded throughout the system and there is no replenishment of this distribution. In this model we include a boundary region containing an enhanced density of thermal plasma with $v_{Tc}/c = 0.01$. In order to represent the extended dimension of the AKR cavity in the longitudinal direction, periodic boundary conditions are assumed in y. This model allows us to examine differences in propagation in directions normal and tangential to the cavity boundary. The width of the enhanced density region on each side of the cavity is typically 128Δ, the density of thermal plasma is 5 or 10 times that of the shell electrons, and the total number of particles ranges up to 26 million.

3. Driven Simulation Results

[14] We consider primarily the case where the initial shell distribution is peaked at an energy of 5 keV. Figure 2 shows a plot of the x component of the Poynting vector at two different times well after the initial transient burst of radiation. (The initial burst peaks at $\Omega_e t \sim 1600$.) The radiation builds up very rapidly with decreasing altitude and reaches a peak at only 5–6 km below the injection line. The RMS electric field amplitude corresponding to this peak power is between 500 and 600 mV/m. At lower altitudes there is no discernible radiation. (The plots in Figure 2 are an average over 1.5 electron cyclotron periods; the instantaneous Poynting vector plots show more structure extending down along the field lines.) The maser instability is thus very efficient at extracting energy from a shell type distribution and converting it into radiation propagating perpendicular to the magnetic field. This is further illustrated in Figure 3, which shows the average perpendicular speed $v_\perp$ as a function of distance below the injection line for simulations with initial shell energies of 3, 5, and 10 keV. In all cases most of the energy is extracted within the first 10 km, and there is essentially no further decrease in particle energy after the first 20 km. For emission at 90°, the resonant ellipse reduces to a circle centered at $v_\parallel = 0$ [*Omidi and Gurnett*, 1982; *Melrose et al.*, 1982; *Dusenbery and Lyons*, 1982], and the shell distribution then has $\partial f/\partial v_\perp > 0$ along the entire downgoing arc. In contrast, the ring beam distribution centered at a downgoing pitch angle of 45° used in the simulations of *Pritchett and Winglee* [1989] resulted in a series of discrete wave packets whose extent along the field was of the order of 3–6 km and which traveled in phase with the drifting electrons. Those wave packets had a significant parallel wave number with $k_\parallel/k_\perp \sim 1/7 \sim v_\parallel/c$. The resonant diffusion of the electrons was much slower, and it required at least 50 km of parallel path length to remove all the perpendicular free energy [*Pritchett*, 1990]. The electron particle distributions $f(v_\parallel, v_\perp)$ in the present simulations are shown in Figure 4 at two different altitudes and at two different positions within the cavity. The rapid diffusion of the shell distribution to smaller values of $v_\perp$ is clearly apparent.

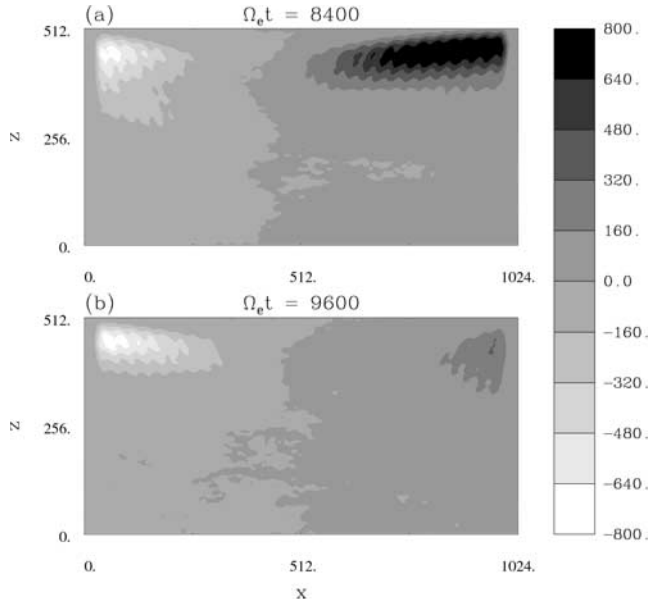

Figure 2. Contours of the x component of the Poynting vector at two different times (a) $\Omega_e t = 8400$ and (b) $\Omega_e t = 9600$ in a driven simulation with 5 keV shell electrons. See color version of this figure at back of this issue.

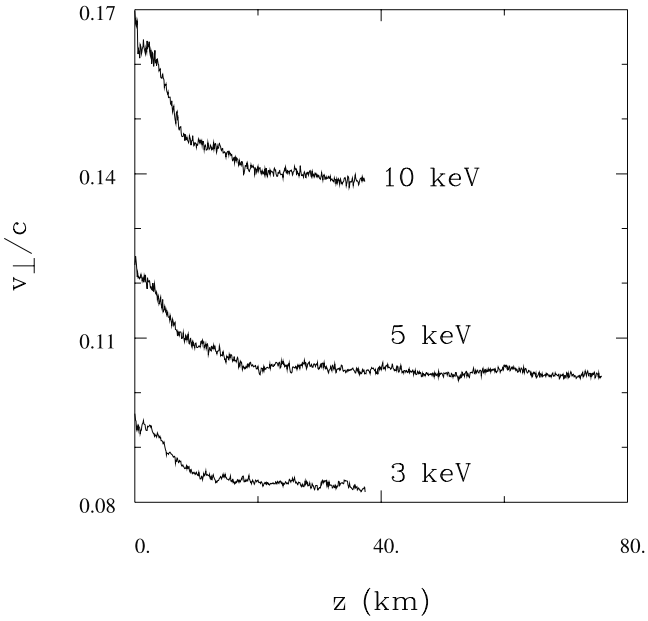

Figure 3. The spatial dependence (as a function of distance below the injection altitude) of the average perpendicular electron speed in driven simulations with initial electron shell energies of 3, 5, and 10 keV.

[15] The radiation emitted by the maser instability has a bursty structure consisting of extended wave packets. Thus in Figure 2b the rightward traveling burst is just exiting the system. This temporal structure is more clearly shown in Figure 5, which presents time histories of the Poynting flux at the boundaries of the simulation domain at several different altitudes. After the initial burst of radiation subsides ($\Omega_e t \sim 1700$), there are subsequent bursts at irregular intervals $\sim 1200\Omega_e^{-1} \sim 0.5$ ms. From Figure 2a it is evident that there is a slight (few degrees) upward refraction of the radiation. This is also shown in Figure 5 where the peaks occur slightly earlier at lower altitudes. The period between bursts varies with the initial shell energy; it is $\approx$0.36 ms for 10 keV and $\approx$0.66 ms for 3 keV (Figure 6). This period appears to be equal to the transit time of the electrons across the $\approx$12 km high generation region. Thus the radiation builds up and relaxes in a quasiperiodic manner as the streaming electrons travel across the generation region. This feature seems to be similar to the fine structure observed on a 1–2 ms timescale by *Strangeway et al.* [2001]. The electric field amplitude during a burst is about 900 mV/m for the 10 keV case and about 300 mV/m for the 3 keV case.

[16] An interesting variation on the present simulation model is shown in Figure 7. Here the density of energetic electrons was doubled in the two regions of width 128Δ demarcated by dashed lines near the two sides of the

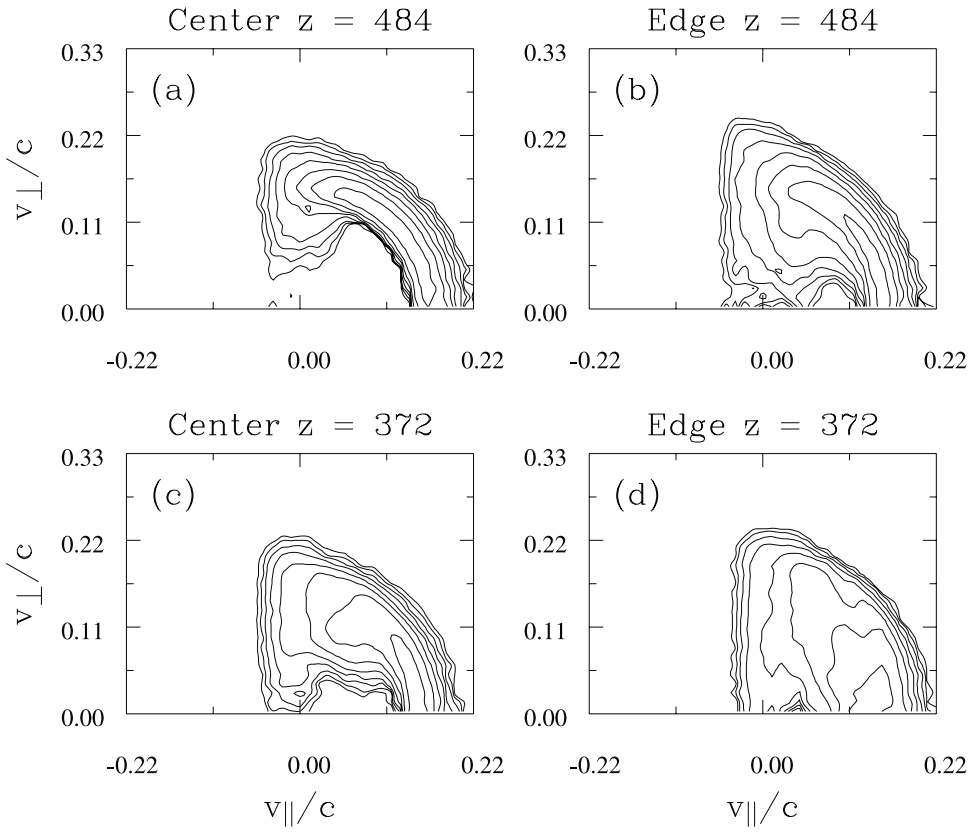

Figure 4. The average electron velocity distribution $f(v_\parallel, v_\perp)$ as measured in a driven simulation with 5 keV shell electrons at two different altitudes $z = 484 \pm 28$ (Figures 4a and 4b) and $z = 372 \pm 28$ (Figures 4c and 4d) and at two different horizontal positions $x = 512 \pm 64$ (Figures 4a and 4c) and $x = 140 \pm 32 \cup x = 864 \pm 32$ (Figures 4b and 4d).

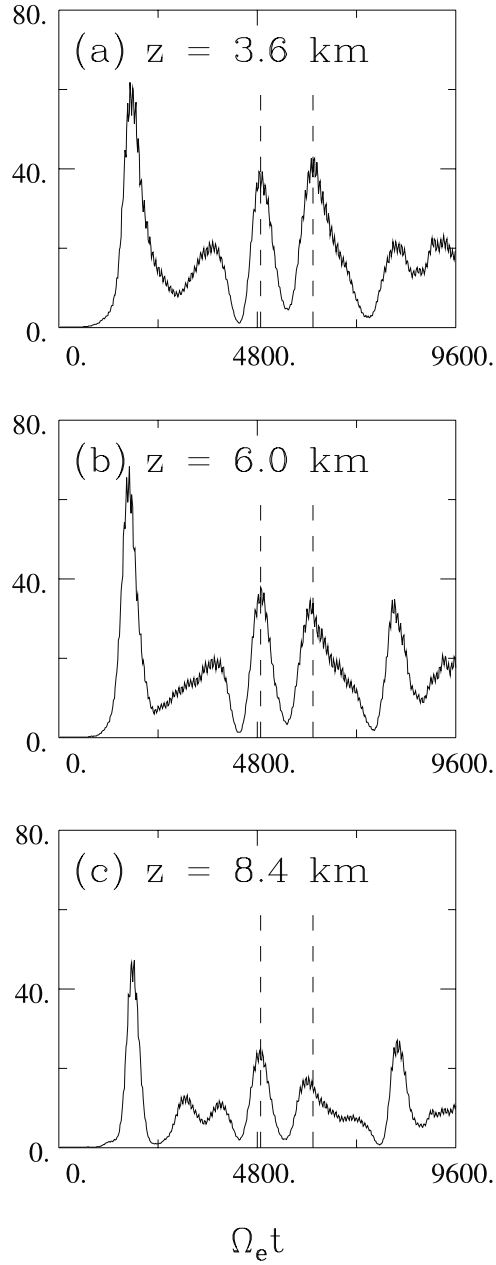

Figure 5. Time history of the Poynting flux measured at the edge of the simulation domain in driven simulations with 5 keV shell electrons for the case of a nonuniform magnetic field strength at distances of 3.6 km (Figure 5a), 6.0 km (Figure 5b), and 8.4 km (Figure 5c) below the injection altitude.

simulation box. Figure 7 shows the x component of the Poynting flux decomposed into the leftward (Figure 7a) and rightward (Figure 7b) traveling components. The color scale is chosen so that the first transition of color on either side of zero occurs at only 2.5% of the peak intensity. Figure 7 shows bursts of radiation crossing each density enhancement. There is no indication, however, of any reflected radiation (at the few percent level) at these sharp density transitions. In fact, the reflected intensity is likely to be much smaller. For a simple 1-D problem in which radiation is incident normally on an interface between two media with indices of refraction n_1 and n_2, application of the continuity conditions to Maxwell's equations at the boundary [*Hayes*, 1985] yields an expected reflected electric field of relative amplitude $R = (n_1 - n_2)/(n_1 + n_2)$. For extraordinary mode waves with frequency near Ω_e and assuming $k_{\|} = 0$, the dispersion relation has the approximate form [*Le Quéau et al.*, 1984; *Pritchett*, 1986a]

$$(1 - n^2) + (2 - n^2)A = 0, \tag{1}$$

where A involves an integration in velocity space of a differential operator acting on the electron velocity distribution function but is otherwise linear in the plasma density. The change δn in the index of refraction resulting from a change $\delta\rho$ in the density is then

$$\delta n = \frac{(n^2 - 1)(2 - n^2)}{2n} \frac{\delta\rho}{\rho}. \tag{2}$$

For n close to 1 ($n \approx 0.99$ for the maser radiation), the reflection coefficient $R \approx (n^2 - 1)(\delta\rho/\rho)/4$. Even for $\delta\rho/\rho = 1$, this yields a fractional reflected energy of only 2.5×10^{-5}. These results thus cast considerable doubt on the

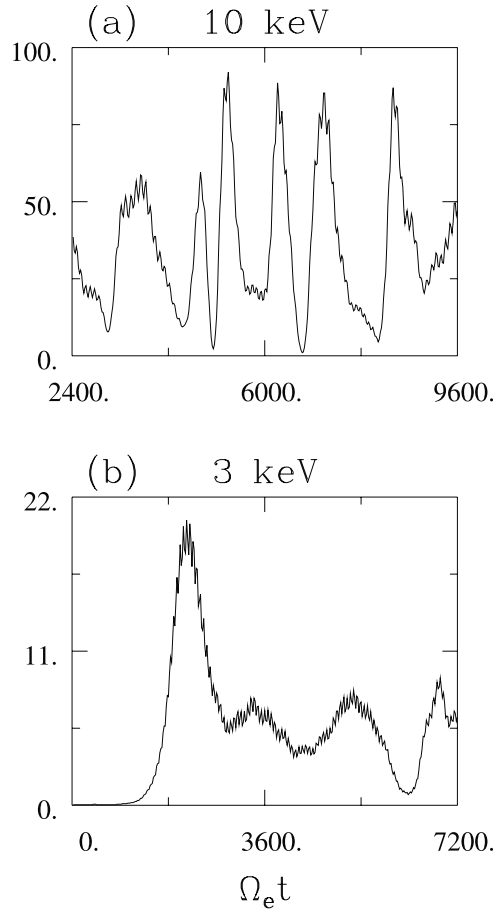

Figure 6. Time history of the Poynting flux measured at the edge of the simulation domain at a distance of 6.0 km below the injection altitude in driven simulations with (a) 10 keV and (b) 3 keV shell electrons.

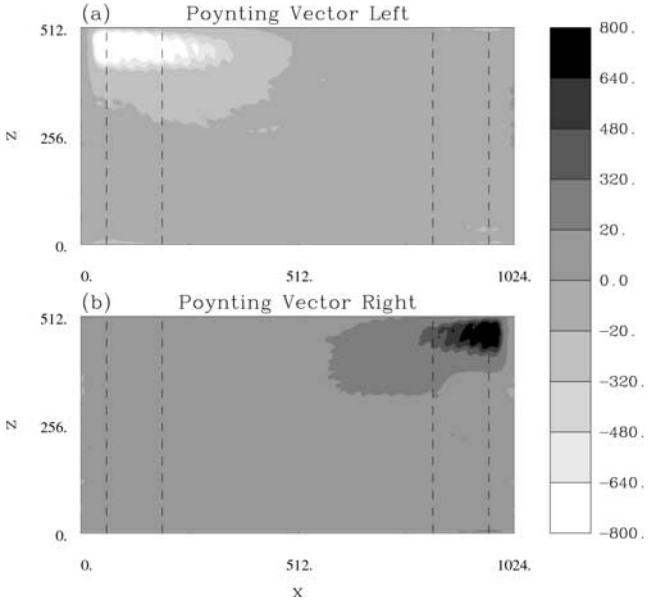

Figure 7. Contours of the x component of the Poynting vector decomposed into its (a) leftward and (b) rightward traveling components. The density of shell electrons within the two regions bounded by dashed vertical lines at the sides of the simulation domain is maintained at twice the value of the density in the central region. See color version of this figure at back of this issue.

validity of the feedback mechanism proposed by *Calvert* [1982, 1987] in which it was argued that partial wave reflection at a moderate density increase within the auroral cavity would lead to radio lasing and the production of a series of extremely narrow bandwidths.

4. The 1-D Cavity Boundary Simulations

[17] Before proceeding to the 2-D bounded cavity simulation model illustrated in Figure 1a, we consider a 1-D model in which the y dependence is ignored and only the spatial coordinate x is considered. All three field and velocity components are retained, however. Then E_x represents the electrostatic field, E_y represents the X mode electromagnetic polarization, and E_z the O mode electromagnetic polarization. This model will permit a simpler discussion of the mode behavior at the cavity boundary. This model is essentially that used by *Pritchett* [1986b].

[18] Figure 8 shows the spatial dependence of the number density and of the fields E_x and E_y at a time $\Omega_e t = 6000$. As indicated in Figure 8a, cold plasma regions of density 10 times that of the energetic plasma are located on both sides of the cavity containing the shell-distribution electrons whose energy is 5 keV. At the sharp density boundary it is clear that there is a change in the electric field polarization. There is an abrupt increase in the electrostatic component (Figure 8b) and a decrease in the X mode component followed by a modulation in its amplitude

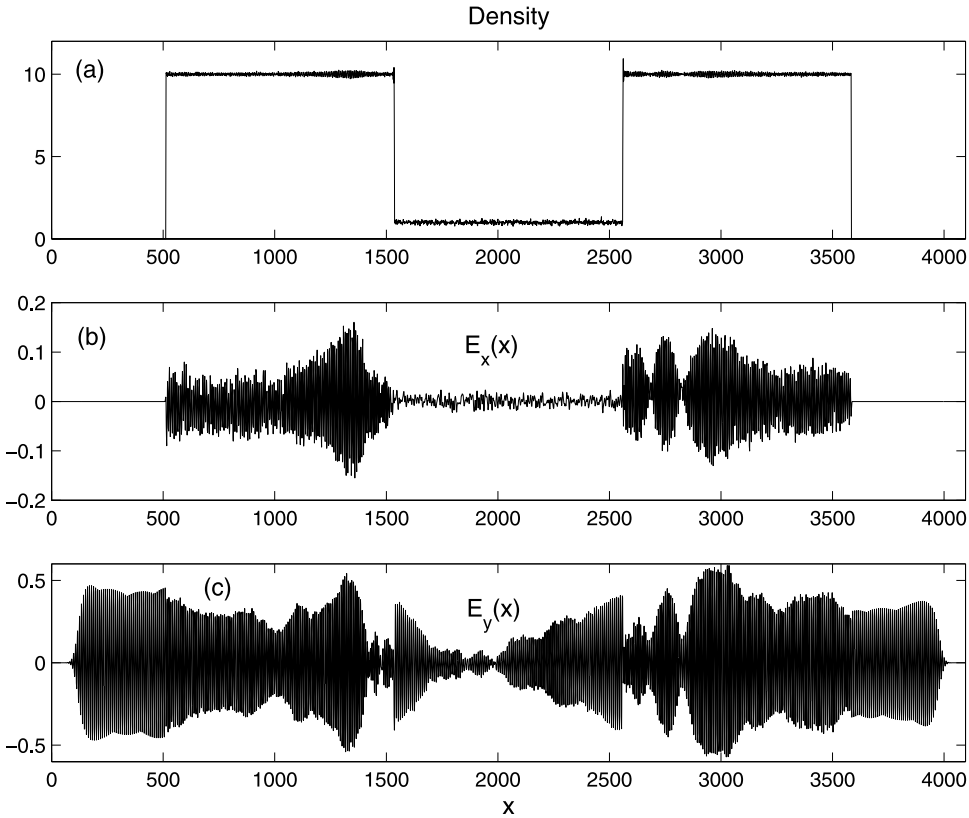

Figure 8. Spatial profiles from a 1-D cavity simulation at a time $\Omega_e t = 6000$ for 5 keV shell electrons. (a) The number density, (b) the electric field E_x, and (c) the electric field E_y.

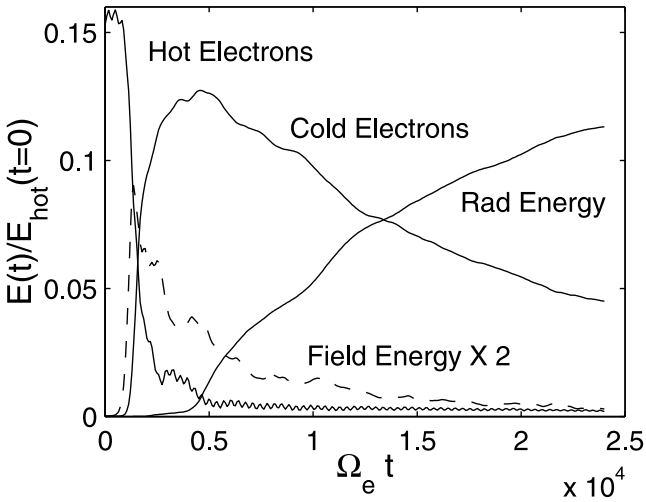

Figure 9. Time history of the kinetic energy of the shell electrons (''Hot Electrons''), of the kinetic energy of the cold ambient electrons on either side of the density cavity (''Cold Electrons''), of the integrated Poynting flux appearing in the vacuum region (''Rad Energy''), and of the total perturbed electric and magnetic field energy (''Field Energy'', multiplied by factor of 2, dashed line). All energies are normalized to the initial kinetic energy of the shell electrons, and the scale of the hot electrons curve has been shifted down so that the peak is 0.16 rather than 1.0.

(Figure 8c). At the discontinuity, the wave number changes from $kc/\Omega_e = 0.99$ to $kc/\Omega_e = 1.11$. This represents a mode conversion from the incident X mode to a Z mode [*Pritchett*, 1986b]; the Z mode has both electrostatic and electromagnetic components. The predicted reflected energy flux at the boundary is only 0.3%. In addition to being partially transmitted, however, the incident X mode radiation is strongly absorbed by the cold plasma near the boundary. Within a wavelength or so of the boundary, the perpendicular distribution of the cold electrons develops a tail extending up to about the original shell energy. In addition, there is some perpendicular bulk heating extending away from the interface. Figure 9 shows time histories of several energy quantities. The energy of the shell electrons decreases very rapidly as the maser instability develops; the net loss is about 15.4% of the initial energy. The field energy in the system ($\int(E^2 + B^2)dx/8\pi$) is shown by the dashed line, which has been multiplied by a factor of two to improve clarity. The field energy grows rapidly at first, reaches a level of 4.5% of the initial shell electron energy, and then decays slowly. The energy of the cold electrons increases as the X mode radiation crosses the cavity boundary, and it reaches a peak level corresponding to 12.7% of the initial shell electron energy. It then decreases slowly as radiation propagates through the cold plasma regions and is eventually removed in the absorbing regions at the two sides of the simulation. Some 75% of the energy lost by the energetic electrons eventually propagates out of the system, but this radiation is no longer coherent.

[19] If the initial energy of the shell electrons is lower, then the maser frequency shifts closer to Ω_e since the relativistic factor γ becomes closer to unity. In this case the transmission of radiation via the Z mode becomes less efficient, and the absorption at the density jump increases. This is illustrated in Figure 10; here the initial electron energy is 2 keV and the density jump is a factor of 5. There is now a sharp spike in E_x at the density enhancement and a pronounced drop in the transmitted E_y amplitude. The absorbed energy in the cold plasma is now almost exclusively concentrated just inside the high-density region and takes the form of a tail on the perpendicular distribution. The maser instability now extracts 9% of the energy of the shell electrons, but only about 30% of this energy has propagated out of the system by a time $\Omega_e t = 1.9 \times 10^4$. For 10 keV shell electrons, the transmission process is much more efficient. For this case 24% of the initial shell electron energy is removed, and about 90% of this propagates out of the system.

[20] Since the wavelength of AKR is of the order of only a kilometer, it may not be realistic to assume a perfectly sharp density discontinuity. (Note, however, that Viking observations did indicate that gradient scale lengths at the edges of cavities could be as low as 1.4 km [*Hilgers et al.*, 1992].) We have thus performed additional simulations in which the discontinuity is replaced by a linear density gradient with a scale much larger than the wavelength. Figure 11 shows a representative case. Here the density change occurs over $256\Delta = 22$ km, and the electron shell energy is 2 keV. There is still a decrease in the E_y amplitude at the start of the linear gradient, but it is less abrupt than in the sharp boundary case of Figure 10. Figure 11c shows that there is a discontinuity in the Poynting vector, indicating that the cold plasma is absorbing energy. This again produces a tail on the perpendicular distribution, this time at the start of the linear gradient region. The amount of hot electron energy extracted by the maser instability and the amount of energy actually propagating out of the system are both somewhat larger (by 25%–40%) with the linear density gradient than with the sharp density jump. The general pattern of mode conversion to the Z mode and absorption by the cold plasma, however, does not seem to be altered fundamentally in the case of the finite density gradient. Also, the actual value of the density jump does not seem to affect the results strongly.

5. The 2-D Cavity Boundary Simulations

[21] With the 2-D simulation model illustrated in Figure 1a it is possible for the maser radiation to propagate both normally and tangentially to the cavity boundary. The X mode radiation propagating in the normal direction has an E_y polarization, while that propagating in the tangential direction has an E_x polarization. In both cases the perturbed magnetic field is in the z direction, parallel to the ambient field. Figure 12 shows time histories of the electric and magnetic field energies E_x^2, E_y^2, and B_z^2 integrated over the entire simulation domain for the cases of shell electrons with 2, 5, and 10 keV and a boundary density enhancement of 5. Also shown is the amount of radiation energy escaping out of the system. All of these energies are normalized to the initial hot electron energy. At 2 keV most of the field energy in all components is retained in the system. At the higher energies the E_y component (normal propagation) is depleted via transmission and absorption, while a significant

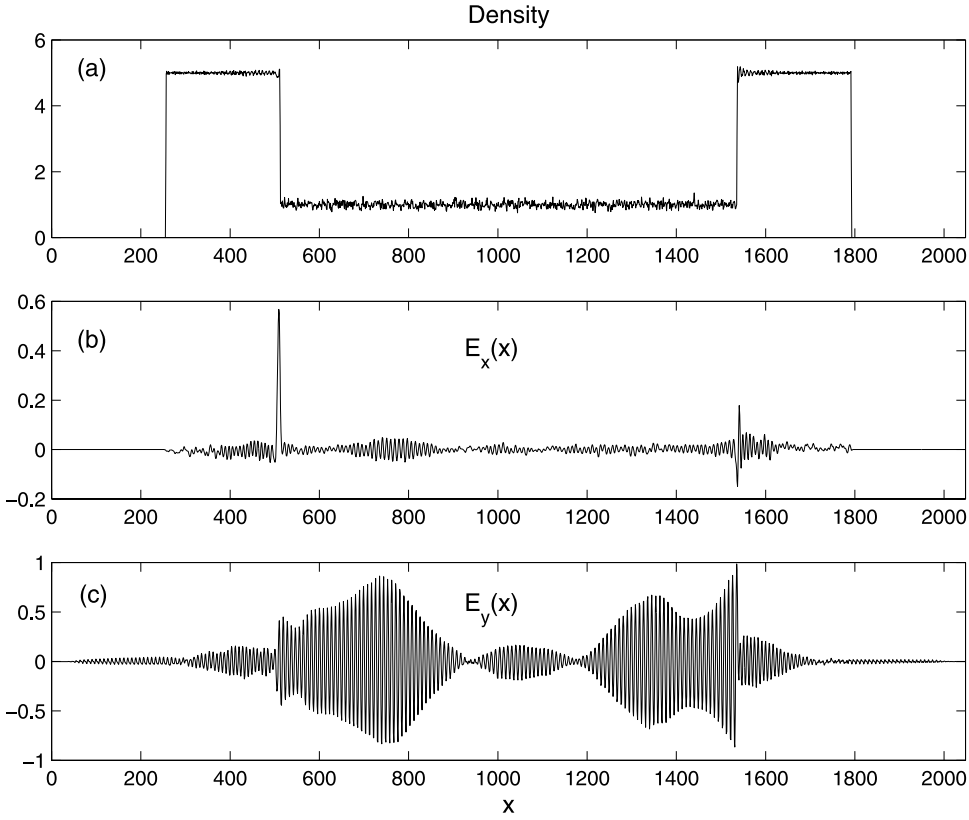

Figure 10. Same as Figure 8 except for 2 keV shell electrons at a time $\Omega_e t = 3200$.

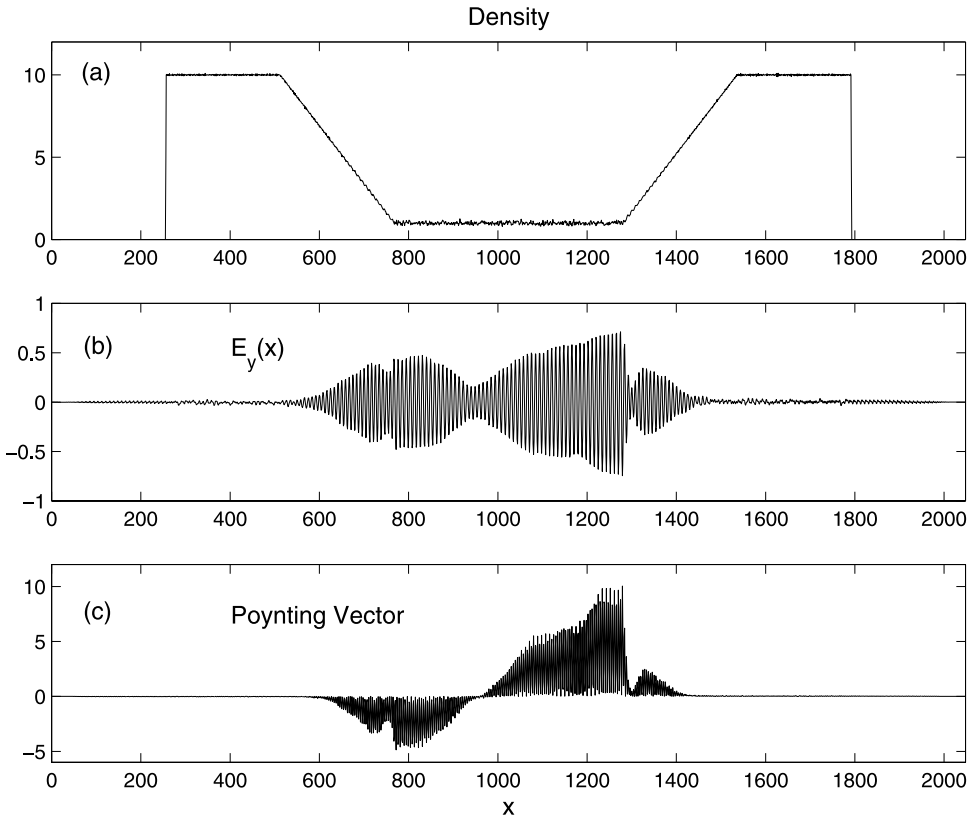

Figure 11. Spatial profiles from a 1-D cavity simulation with linear density gradient at a time $\Omega_e t = 2400$ for 2 keV shell electrons. (a) The number density, (b) the electric field E_y, and (c) the x component of the Poynting vector.

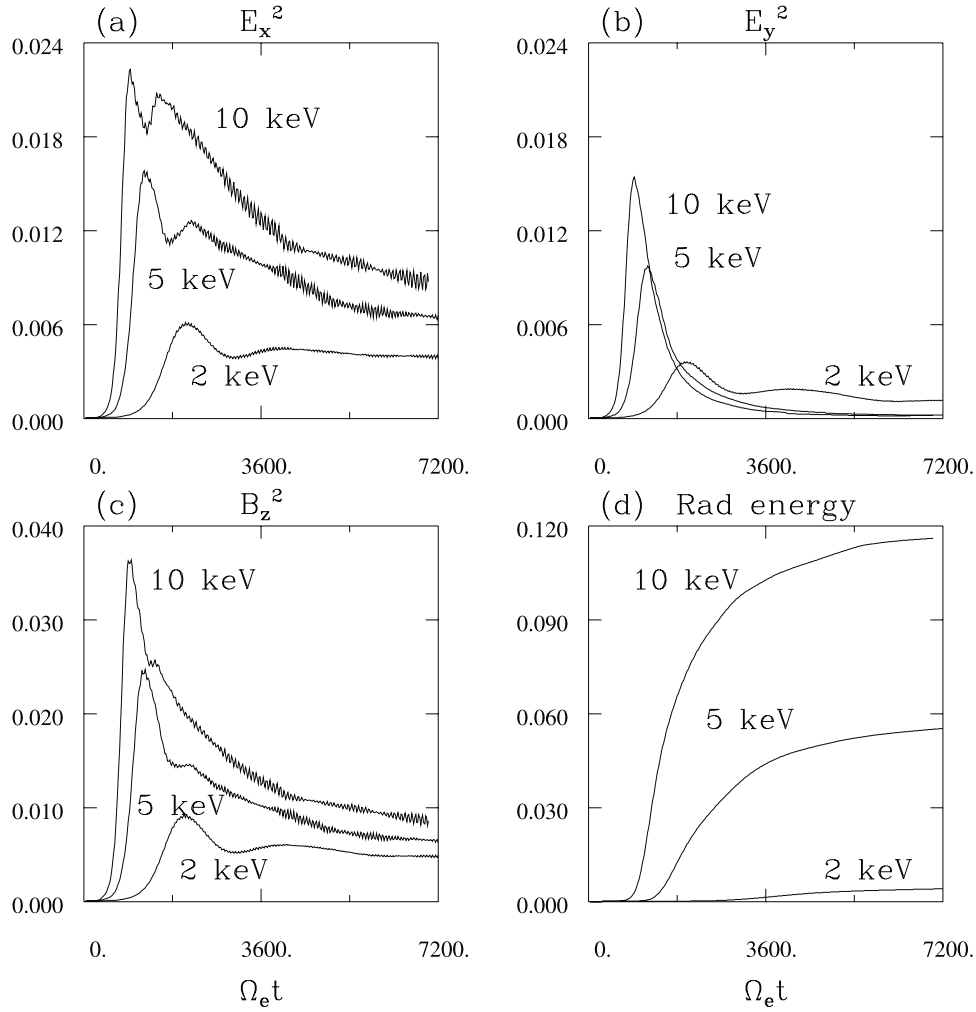

Figure 12. Time history of (a) the total electric field energy E_x^2, (b) the total electric field energy E_y^2, (c) the total perturbed magnetic field energy B_z^2, and (d) the total Poynting flux appearing in the vacuum regions for 2-D cavity simulations with initial electron shell energies of 2, 5, and 10 keV.

fraction of the E_x component (tangential propagation) remains in the system. In these simulations the width in x of the energetic plasma region is $640\Delta = 54$ km, while the system is unbounded in y as a result of the assumption of periodic boundary conditions. Since the peak E_y^2 energies are nearly as large as the corresponding E_x^2 energies ($\sim$65%), this width is evidently sufficient to extract most of the free energy from the shell electrons.

[22] Figure 13 shows the Poynting vector for the 2 keV (Figure 13a) and 10 keV (Figure 13b) cases. For the lower energy the Poynting flux impinges on the boundary but does not penetrate through. There is again considerable energy absorption by the cold plasma with the formation of a perpendicular tail. In contrast, for the higher energy there is considerable direct penetration. Figure 14 shows (for the case of 5 keV shell electrons) that the perpendicular energization of the cold plasma extends several wavelengths away from the interface. In all the cases the radiation is seen to be filamented into thin structures of size 1–2 km.

[23] In a full 3-D geometry the maser radiation would refract upward in the presence of the magnetic field gradient [*Le Quéau et al.*, 1985; *Zarka et al.*, 1986; *Pritchett and Winglee*, 1989; *Louarn and Le Quéau*, 1996a, 1996b]. The evolution of time in the present 2-D initial value simulations is qualitatively similar to the propagation to higher altitudes in the 3-D geometry. Thus, with the possible exception of low-energy electrons, as the radiation refracts upward, it should be increasingly dominated by the tangential component. As suggested by *Louarn and Le Quéau* [1996b], this component can directly couple to the free space X mode when the cyclotron frequency has decreased sufficiently so that the external X mode cutoff becomes smaller than the maser wave frequency.

[24] Viking observations [*Louarn and Le Quéau*, 1996a] reported extremely low levels of Z mode radiation outside of the source region. To avoid the efficient coupling of the X mode to the Z mode across the boundary, it was proposed [*Louarn and Le Quéau*, 1996b] that AKR is generated in thin regions of only a few kilometers width in the normal direction. The radiation would then be produced primarily in a direction tangential to the boundary. Figures 15 and 16 show simulation results for a case where the cavity width is only 128Δ (11 km). The tangentially propagating field energy (E_x^2) is now much larger (by a factor of 10) than

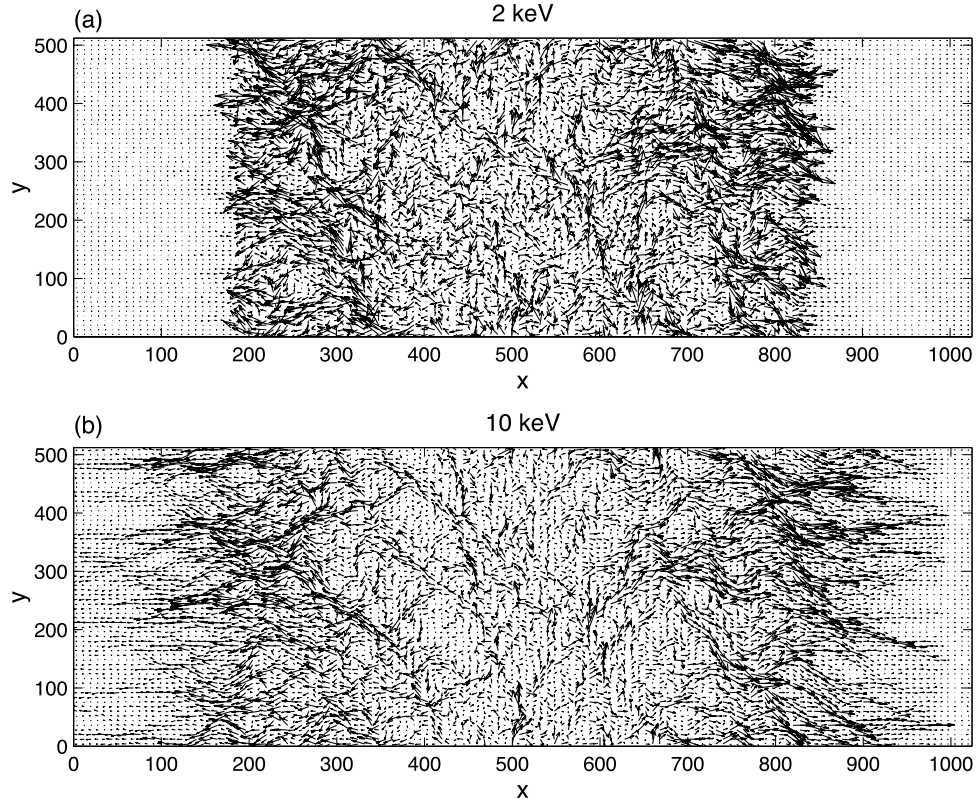

Figure 13. Arrow plots of the Poynting vector in 2-D cavity simulations for the cases of (a) an initial electron shell energy of 2 keV (at time $\Omega_e t = 2400$) and (b) an initial electron shell energy of 10 keV (at time $\Omega_e t = 1000$).

the normal radiation (E_y^2), and the Poynting flux is indeed dominated by the y component.

6. FAST Observations of Electric Field Polarization

[25] After deployment of the boom axis antenna (which occurred during orbit 1795), it is possible to determine all three components of the electric field for intervals with high-speed burst memory (HSBM) data. The HSBM data are short bursts of waveform data sampled at 2×10^6 samples per second. A single burst interval typically lasts for ~260 ms. The booms consist of three spin-plane wire booms, and a spin-axis boom. See *Ergun et al.* [2001] for a complete description of the FAST fields experiment.

[26] Of the AKR source region crossings previously studied by *Ergun et al.* [1998] and *Delory et al.* [1998], only that during orbit 1907 occurred after the boom deployment and possessed suitable HSBM data. These data exist near 18:58:56.3 UT, which corresponds to the equatorward edge of the second density cavity described by Ergun et al. In this cavity, which was about 36 km wide, there were ~1 to ~10 keV precipitating electrons, no electron fluxes below ~1 keV (apart from spacecraft photoelectrons), upgoing ion beams of ~0.5 keV to ~1 keV at the edge and reaching several keV further into the cavity, and strong AKR emissions reaching down to Ω_e. Figure 17a shows the power in the three electric field polarizations (one parallel to the ambient magnetic field, two perpendicular with polarizations either along or across the spacecraft trajectory) as a function of frequency. The power in all three components is strongly enhanced beginning at ~430 kHz, with the peak occurring at ≈435 kHz; the electron cyclotron frequency is ≈433 kHz. At the peak, the power in the along-track polarization is a factor of ~100 greater than that in the across-track polarization. A maximum variance analysis of a short interval of burst waveform data in this AKR emission range yields an angle $\theta_{E,B} = 85°$ and an azimuth angle $\phi = 3.4°$ ($\phi = 0$ corresponds to electric field along track, $\phi = 90°$ to across track). The maximum variance analysis determines the angles that yield maximum wave power in the electric field. These data together with the observation that the wave magnetic field is polarized parallel to the ambient magnetic field [*Ergun et al.*, 2000; *Strangeway et al.*, 2001] indicate that the wave is an X-mode wave with the wave vector perpendicular to the ambient field and spacecraft velocity vector.

[27] Figures 18 and 19 show survey plots for two additional crossings, during orbits 12639 and 12745. Figures 17b and 17c show the corresponding power versus frequency spectra for the three electric field polarizations. For orbit 12639 the HSBM data coincide with a short burst (~2 s) of AKR and the crossing of a narrow (~8 km) cavity which again is characterized by a drop out of electron flux below ~1 keV and an upgoing ion beam of a few keV. The along-track polarization begins to exceed the across track at ~350 kHz, and both polarizations intensify rapidly above $\Omega_e \approx 368$ kHz. The peak power occurs in the range of 372–376 kHz, with the along-track component dominant by a factor of ≈20 near the lower end

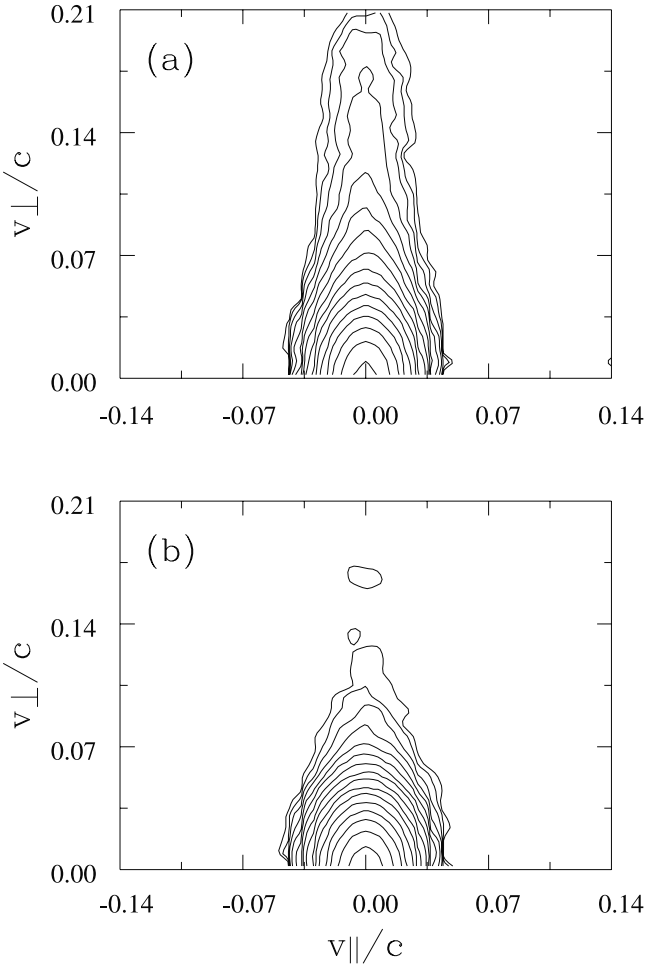

Figure 14. The average electron velocity distribution $f(v_{\|}, v_{\perp})$ at time $\Omega_e t$ = 2400 as measured in a 2-D cavity simulation with 5 keV shell electrons for (a) a region encompassing the first 32 cells in the boundary regions (measured outward from the density jump) and (b) a region encompassing cells 33–64 in the boundary regions (measured outward from the density jump). The value of f changes by a factor of 2 between successive contours.

of this range. The maximum variance analysis yields $\theta_{E,B}$ = 88° and ϕ = 2°.

[28] For orbit 12745 the frequency spectrum shows two primary peaks (~349 kHz and ~367 kHz) and a weaker peak (~340 kHz) at or above Ω_e. These peaks are about a factor of 10 or more weaker than for the previous two examples. Here the two perpendicular polarizations are about equal, with $\phi = -137°$. The parallel component is quite small at the lowest frequency peak but becomes more significant at the two higher frequencies. The HSBM data occur near the poleward edge of an ~65 km wide cavity. There is again a pronounced multikeV upgoing ion beam, but the AKR intensity was stronger earlier in the cavity.

[29] The polarization spectra for the three AKR source crossings presented in Figure 17 are typical based on a survey of some 10 crossings. (As noted above, HSBM bursts are typically ~260 ms long, and at most three or four bursts are acquired per orbit. As a consequence, the occurrence of HSBM data is often not well correlated with strong AKR emissions. Of the approximately 150 orbits surveyed around orbit 12700, there were only 6 candidate HSBM intervals.) The electric field vector is always nearly perpendicular to the ambient magnetic field, as had been established previously from spin plane data alone. Of the two perpendicular polarizations, the along track component is comparable to, or frequently considerably stronger than, the across-track component. This dominance of the along-track orientation is particularly apparent for the stronger intensity AKR cases. No examples were found where the across-track polarization was larger. Thus these observations support the simulation results that the across-track component should leak out of the cavity and that AKR in the source region should propagate predominantly in the longitudinal direction. An additional implication of these observations is that the AKR emissions do not form a standing wave structure between the cavity boundaries.

7. Summary and Discussion

[30] We have investigated a number of issues associated with the generation and propagation of electron-cyclotron

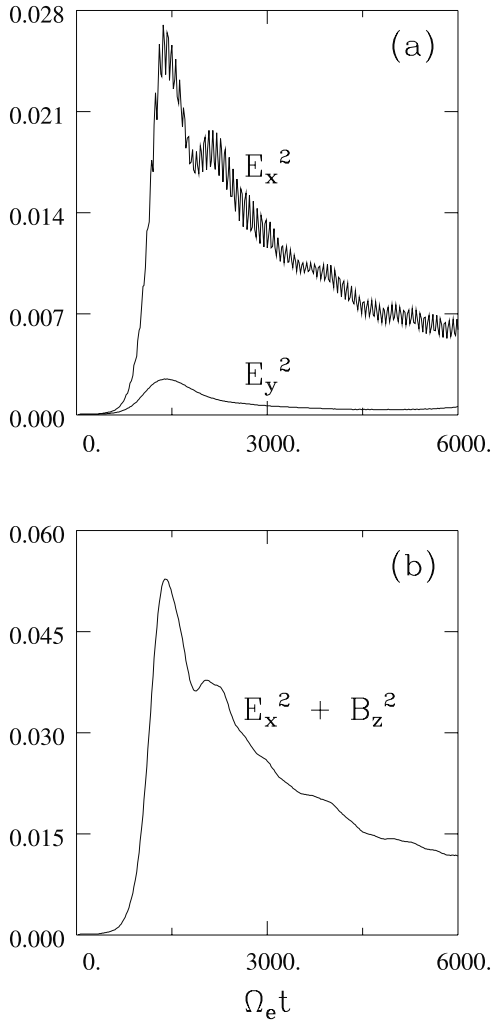

Figure 15. Time history of (a) the total electric field energies E_x^2 and E_y^2 and (b) the total perturbed field energy $E_x^2 + B_z^2$ in a 2-D cavity simulation with 5 keV shell electrons and a narrow cavity width of 128Δ.

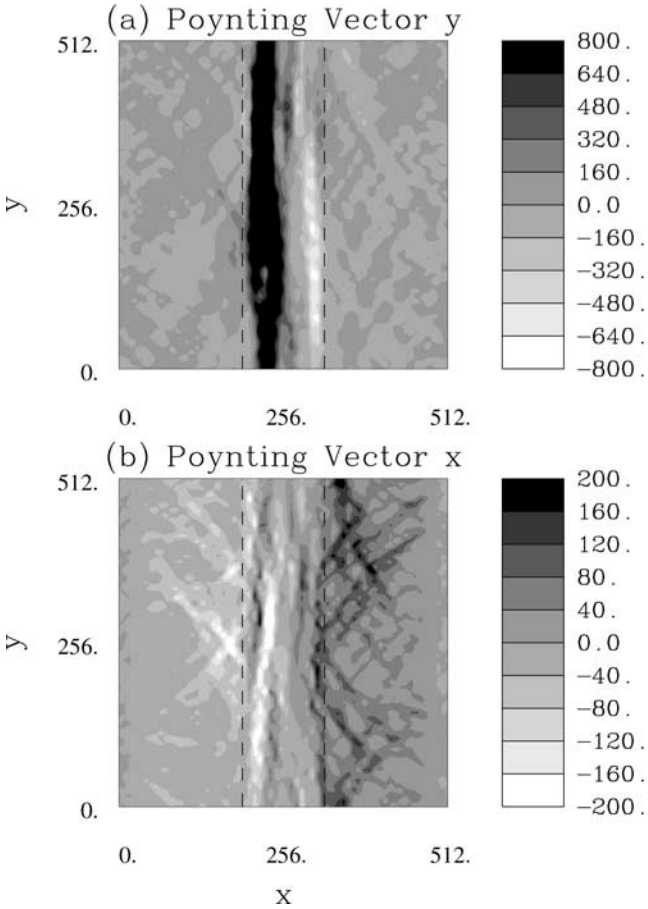

Figure 16. The (a) y and (b) x components of the Poynting vector at time $\Omega_e t = 1600$ for a narrow cavity simulation with 5 keV shell electrons. See color version of this figure at back of this issue.

maser emissions within a finite source cavity such as that characterizing the AKR source region. We have employed two 2-D PIC simulation models to study propagation in a meridional and a longitudinal plane. In both cases the free-energy source for the maser emissions was a dilute ($\omega_{pe} \ll \Omega_e$) population of primary auroral electrons with a downgoing shell distribution, as suggested by recent FAST observations.

[31] The simulation results indicate that the maser radiation component incident normally on the cavity boundary (with across-track E polarization) tends to leak out of the cavity via conversion to the Z mode and absorption by the ambient cold plasma. This destroys the coherency of this component. In contrast, the component propagating in the longitudinal direction (with along-track E polarization) is free to grow along an extended path length. The FAST observations of the electric field in the source region demonstrate that the polarization in the plane perpendicular to **B** varies between being isotropic to having a substantial enhancement of the along-track polarization. No evidence was found that the across-track polarization was ever dominant. One can thus conclude that AKR does not form a standing wave structure between the cavity boundaries.

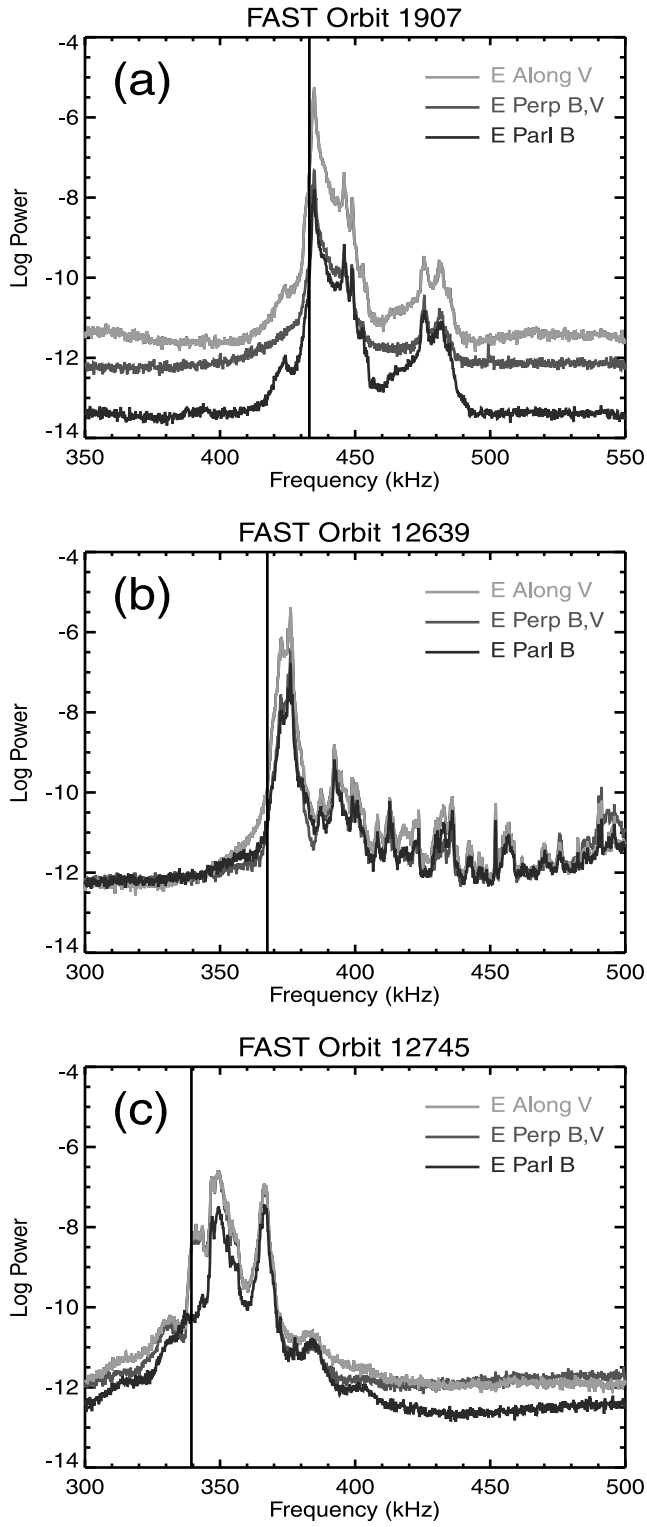

Figure 17. Power spectra for the three electric field components as determined from FAST crossings of the AKR source region on (a) orbit 1907 near 23 MLT, (b) orbit 12639 near 21 MLT, and (c) orbit 12745 near 21 MLT. The two perpendicular field components have been projected along directions parallel to the spacecraft trajectory and perpendicular to both B and the trajectory. In all panels the vertical solid line indicates the (nonrelativistic) electron cyclotron frequency. See color version of this figure at back of this issue.

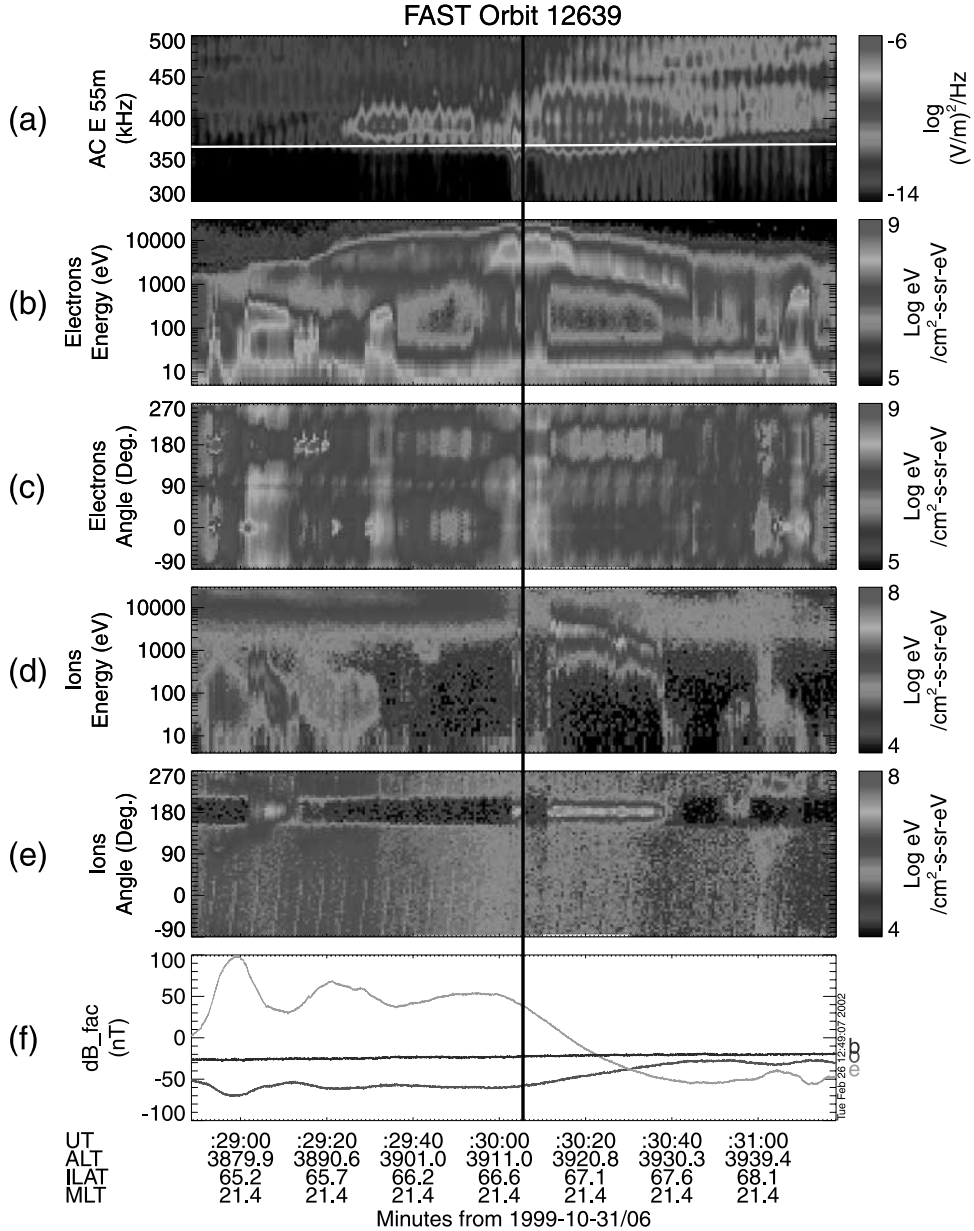

Figure 18. Particle and field data acquired by FAST on orbit 12639. (a) Electric field data in the frequency range 300–500 kHz. The white trace gives the local electron gyrofrequency. (b) Electron energy flux versus energy and time. (c) Electron energy flux versus pitch angle and time. (d) Ion energy flux versus energy and time. (e) Ion energy flux versus pitch angle and time. (f) The deviation of the observed magnetic field from the model field (IGRF 95) in field-aligned coordinates: outward (o), eastward (e), and model-field aligned (b). The vertical black line indicates the interval of HSBM data. See color version of this figure at back of this issue.

[32] The dominance of the along-track polarization had been suggested previously by *Louarn and Le Quéau* [1996a, 1996b] based on indirect evidence from Viking observations and a model for the coupling of maser radiation modes across the cavity boundary. They suggested that AKR generation occurs in subcavities with transverse width of only a few km. Then amplification by the maser instability is possible only in the longitudinal direction. The present FAST observations of isotropic electric field polarization in some cases demonstrates that this subcavity scenario is not always correct. An alternative explanation for the cases of dominant along-track polarization is that while isotropic amplification of the maser radiation occurs throughout most of the 30–100 km wide source cavity, the across-track component propagating normal to the cavity leaks out of the cavity and is lost, leaving the along-track component to be dominant and escape at higher altitudes.

[33] To distinguish between these two mechanisms leading to a dominant along-track polarization, one needs high-resolution observations just outside the main source cavity. The Viking observations [*Louarn and Le Quéau*, 1996a]

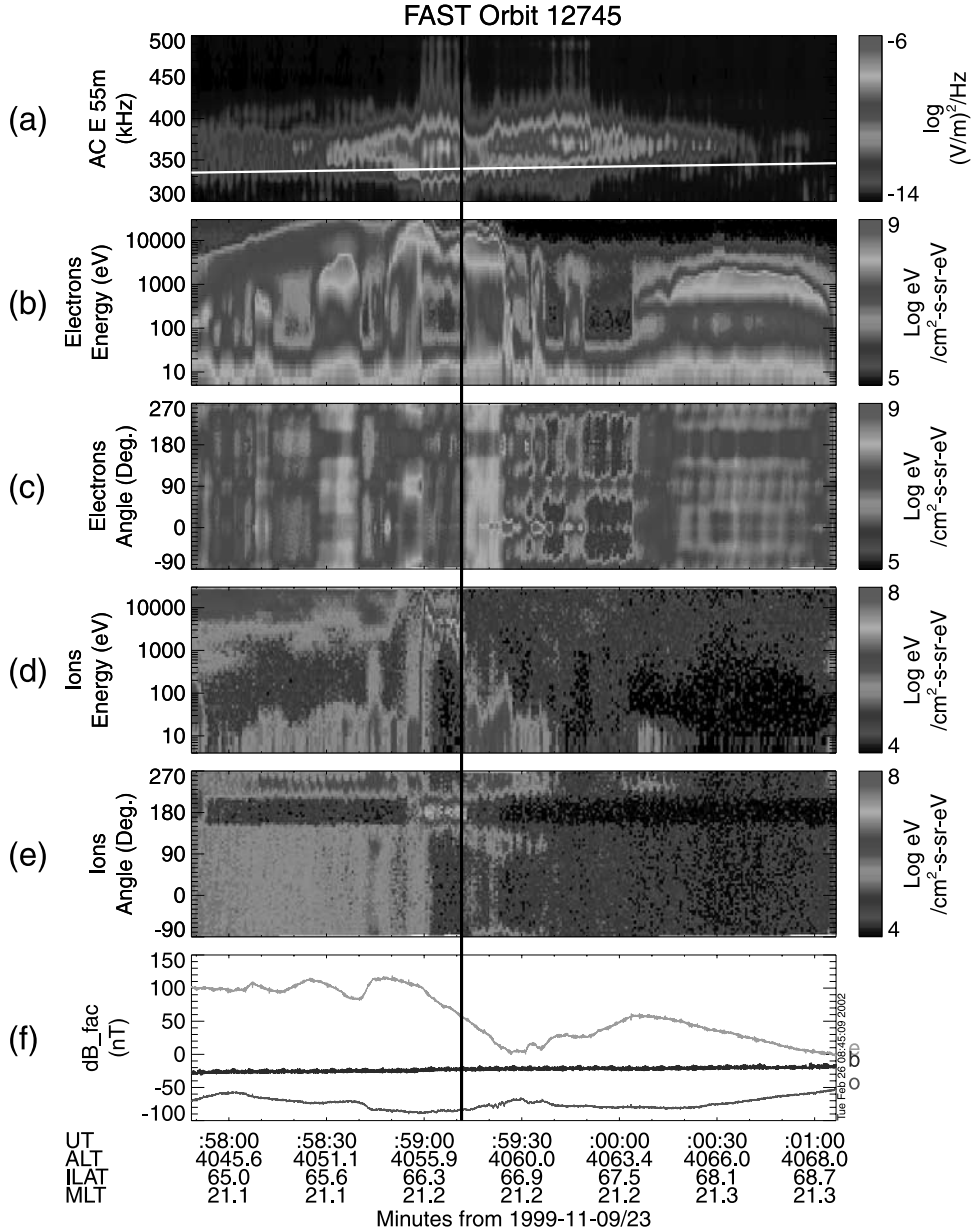

Figure 19. Same as Figure 18 but for orbit 12745. See color version of this figure at back of this issue.

indicated very low levels of Z mode radiation outside the source, but since the mode conversion process involves such a small change in the wave number ($\Delta k/k \sim 10\%$), it is difficult to distinguish between Z and X modes. A more conclusive demonstration could be furnished by the particle distributions. The present simulations have shown that there is significant perpendicular heating of the thermal electrons in the region outside the source cavity due to absorption of the maser radiation. Thus there should be a significant $T_\perp > T_{||}$ anisotropy just outside of the cavity. This, however, is also an inherently difficult measurement. First, the anisotropy region is only a few km wide and is thus covered in a timescale of the order of a second or less; only a few particle spectra are acquired in this transition region. Second, in addition to any possible transverse heating, the electrons in the transition region have also been processed differently along the field. In particular, the transition region is not only associated with a perpendicular gradient, it is also a boundary between a location where the observations are acquired within the auroral acceleration region and one where the auroral acceleration is entirely above the spacecraft. Nevertheless, it would be worthwhile to perform a systematic survey of the edges of the auroral cavity as observed by FAST, but this is beyond the scope of the present work, which has concentrated on the polarization of AKR within the cavity.

[34] Since the AKR radiation is likely to propagate primarily in the longitudinal direction, it appears that previous concerns regarding insufficient path length and amplification are not warranted. With perpendicular emission in this direction, the magnetic field inhomogeneity is not a limiting factor. Likewise, there is no need to appeal to

repeated traversals of the source region resulting from partial reflections at density gradients to enhance the amplification. The simulations indicated that any such reflections are quite weak, so that the conditions for a laser mechanism are unlikely to be satisfied. Furthermore, given the longitudinal propagation, there seems little doubt but that the radiation will escape from the cavity at altitudes somewhat above the source region where the local R-X mode cutoff has dropped below the wave frequency.

[35] The origin of the AKR fine structure is still open to question. It seems clear from the present simulations and earlier linear theory evaluations that the basic maser instability produces narrow bandwidths of the order of $\Delta\omega/\Omega_e \sim 1-2 \times 10^{-3}$. This is close to, but not quite as low as, the observations. Likewise, it is still not clear why there are a series of relatively discrete emissions occurring at many different altitudes. The full resolution of this issue will probably require a more detailed source model including the presence of a minority density colder electron species and the inclusion of ion dynamics.

[36] **Acknowledgments.** The research of PLP was supported by NASA grant NAG 5-8060, and the research of the FAST members was supported by NASA grant NAG 5-3596. The particle simulations were performed at the San Diego Supercomputer Center, which is supported by the National Science Foundation, and at the National Energy Research Scientific Computing Center at the Lawrence Berkeley National Laboratory.

[37] Arthur Richmond thanks R. Bingham and Raymond Pottelette for their assistance in evaluating this paper.

References

Baumback, M. M., and W. Calvert, The minimum bandwidths of auroral kilometric radiation, *Geophys. Res. Lett.*, *14*, 119, 1987.

Bingham, R., and R. A. Cairns, Generation of auroral kilometric radiation by electron horseshoe distributions, *Phys. Plasmas*, *7*, 3089, 2000.

Calvert, W., The auroral plasma cavity, *Geophys. Res. Lett.*, *8*, 919, 1981.

Calvert, W., A feedback model for the source of auroral kilometric radiation, *J. Geophys. Res.*, *87*, 8199, 1982.

Calvert, W., Auroral precipitation caused by auroral kilometric radiation, *J. Geophys. Res.*, *92*, 8792, 1987.

Chiu, Y. T., and M. Schulz, Self-consistent particle and parallel electrostatic field distributions in the magnetospheric-ionospheric auroral region, *J. Geophys. Res.*, *83*, 629, 1978.

Dawson, J. M., Particle simulation of plasmas, *Rev. Mod. Phys.*, *55*, 403, 1983.

de Feraudy, H., A. Bahnsen, and M. Jespersen, Observations of nightside and dayside auroral kilometric radiation with Viking, in *Proceedings of 2nd International Workshop on Radio Emissions from Planetary Magnetospheres*, edited by H. O. Rucker, S. J. Bauer, and B. M. Pedersen, p. 239, Österreichischen Akad. der Wiss., Vienna, 1988.

Delory, G. T., R. E. Ergun, C. W. Carlson, L. Muschietti, C. C. Chaston, W. Peria, J. P. McFadden, and R. J. Srangeway, FAST observations of electron distributions within AKR source regions, *Geophys. Res. Lett.*, *25*, 2069, 1998.

Dusenbery, P. B., and L. R. Lyons, General concepts on the generation of auroral kilometric radiation, *J. Geophys. Res.*, *87*, 7467, 1982.

Ergun, R. E., et al., FAST satellite wave observations in the AKR source region, *Geophys. Res. Lett.*, *25*, 2061, 1998.

Ergun, R. E., C. W. Carlson, J. P. McFadden, G. T. Delory, R. J. Strangeway, and P. L. Pritchett, Electron-cyclotron maser driven by charged-particle acceleration from magnetic field-aligned electric fields, *Astrophys. J.*, *538*, 456, 2000.

Ergun, R. E., et al., The FAST satellite fields instrument, *Space Sci. Rev.*, *98*, 67, 2001.

Gary, D. E., J. L. Linsky, and G. A. Dulk, An unusual microwave flare with 56 second oscillations on the M dwarf L726-8 A, *Astrophys. J.*, *263*, L79, 1982.

Gurnett, D. A., and R. R. Anderson, The kilometric radio emission spectrum: Relation to auroral acceleration processes, in *Physics of Auroral Arc Formation*, *Geophys. Monogr. Ser.*, vol. 25, edited by S.-I. Akasofu, and J. R. Kan, p. 341, AGU, Washington, D. C., 1981.

Gurnett, D. A., R. R. Anderson, F. L. Scarf, R. W. Fredricks, and E. J. Smith, Initial results from the ISEE 1 and 2 plasma wave investigation, *Space Sci. Rev.*, *23*, 1079, 1979.

Hayes, L. M., Reflection of magnetoionic waves from a steep density gradient, 1, Incident extraordinary mode, *Aust. J. Phys.*, *38*, 687, 1985.

Hilgers, A., B. Holback, G. Holmgren, and R. Boström, Probe measurements of low plasma densities with applications to the auroral acceleration region and auroral kilometric radiation sources, *J. Geophys. Res.*, *97*, 8631, 1992.

Le Quéau, D., R. Pellat, and A. Roux, Direct generation of the auroral kilometric radiation by the maser synchrotron instability: An analytical approach, *Phys. Fluids*, *27*, 247, 1984.

Le Quéau, D., R. Pellat, and A. Roux, The maser synchrotron instability in an inhomogeneous medium: Application to the generation of the auroral kilometric radiation, *Ann. Geophys. Gauthier Villars*, *3*, 273, 1985.

Louarn, P., and D. Le Quéau, Generation of the auroral kilometric radiation in plasma cavities, I, Experimental study, *Planet. Space Sci.*, *44*, 199, 1996a.

Louarn, P., and D. Le Quéau, Generation of the auroral kilometric radiation in plasma cavities, II, The cyclotron maser instability in small size sources, *Planet. Space Sci.*, *44*, 211, 1996b.

Melrose, D. B., and G. A. Dulk, Electron-cyclotron masers as the source of certain solar and stellar radio bursts, *Astrophys. J.*, *259*, 844, 1982.

Melrose, D. B., K. G. Rönnmark, and R. G. Hewitt, Terrestrial kilometric radiation: The cyclotron theory, *J. Geophys. Res.*, *87*, 5140, 1982.

Omidi, N., and D. A. Gurnett, Growth rate calculations of auroral kilometric radiation using the relativistic resonance condition, *J. Geophys. Res.*, *87*, 2377, 1982.

Omidi, N., and D. A. Gurnett, Path-integrated growth of auroral kilometric radiation, *J. Geophys. Res.*, *89*, 10,801, 1984.

Perraut, S., H. de Feraudy, A. Roux, P. M. E. Décréau, J. Paris, and L. Matson, Density measurements in key regions of the Earth's magnetosphere: Cusp and auroral region, *J. Geophys. Res.*, *95*, 5997, 1990.

Pottelette, R., R. A. Treumann, and M. Berthomier, Auroral plasma turbulence and the cause of auroral kilometric radiation fine structure, *J. Geophys. Res.*, *106*, 8465, 2001.

Pritchett, P. L., Relativistic dispersion, the cyclotron maser instability, and auroral kilometric radiation, *J. Geophys. Res.*, *89*, 8957, 1984.

Pritchett, P. L., Electromagnetic particle simulation codes, in *Space Plasma Simulations*, edited by M. Ashour-Abdalla and D. A. Dutton, p. 17, D. Reidel, Norwell, Mass., 1985.

Pritchett, P. L., Electron-cyclotron maser instability in relativistic plasmas, *Phys. Fluids*, *29*, 2919, 1986a.

Pritchett, P. L., Cyclotron maser radiation from a source structure localized perpendicular to the ambient magnetic field, *J. Geophys. Res.*, *91*, 13,569, 1986b.

Pritchett, P. L., Auroral kilometric radiation: An example of relativistic wave-particle interaction in geoplasma, in *Physics of Space Plasmas 1989*, *SPI Conf. Proc. Reprint Ser.*, vol. 9, edited by T. Chang, G. B. Crew, and J. R. Jasperse, p. 319, Scientific, Gainesville, Fla., 1990.

Pritchett, P. L., and R. J. Strangeway, A simulation study of kilometric radiation generation along an auroral field line, *J. Geophys. Res.*, *90*, 9650, 1985.

Pritchett, P. L., and R. M. Winglee, Generation and propagation of kilometric radiation in the auroral plasma cavity, *J. Geophys. Res.*, *94*, 129, 1989.

Pritchett, P. L., R. J. Strangeway, C. W. Carlson, R. E. Ergun, J. P. McFadden, and G. T. Delory, Free energy sources and frequency bandwidth for the auroral kilometric radiation, *J. Geophys. Res.*, *104*, 10,317, 1999.

Roux, A., A. Hilgers, H. de Feraudy, D. Le Quéau, P. Louarn, S. Perraut, A. Bahnsen, M. Jespersen, E. Ungstrep, and M. Andre, Auroral kilometric radiation sources: In situ and remote observations from Viking, *J. Geophys. Res.*, *98*, 11,657, 1993.

Sharma, R. R., L. Vlahos, and K. Papadopoulos, The importance of plasma effects on electron-cyclotron maser emission from flaring loops, *Astron. Astrophys.*, *112*, 377, 1982.

Strangeway, R. J., Wave dispersion and ray propagation in a weakly relativistic electron plasma: Implications for the generation of auroral kilometric radiation, *J. Geophys. Res.*, *90*, 9675, 1985.

Strangeway, R. J., et al., FAST observations of VLF waves in the auroral zone: Evidence of very low plasma densities, *Geophys. Res. Lett.*, *25*, 2065, 1998.

Strangeway, R. J., R. E. Ergun, C. W. Carlson, J. P. McFadden, G. T. Delory, and P. L. Pritchett, Accelerated electrons as the source of the auroral kilometric radiation, *Phys. Chem. Earth C*, *26*, 145, 2001.

Tsai, S. T., C. S. Wu, Y. D. Wang, and S. W. Kang, Dielectric tensor of a weakly relativistic, nonequilibrium, and magnetized plasma, *Phys. Fluids*, *24*, 2186, 1981.

Winglee, R. M., Interrelation between azimuthal bunching and semi-relativistic maser cyclotron instabilities, *Plasma Phys.*, *25*, 217, 1983.

Winglee, R. M., and P. L. Pritchett, The generation of low-frequency electrostatic waves in association with auroral kilometric radiation, *J. Geophys. Res.*, *91*, 13,531, 1986.

Wong, H. K., C. S. Wu, F. J. Ke, R. S. Schneider, and L. F. Ziebell, Electromagnetic cyclotron-loss-cone instability associated with weakly relativistic electrons, *J. Plasma Phys.*, *28*, 503, 1982.

Wu, C. S., and L. C. Lee, A theory of the terrestrial kilometric radiation, *Astrophys. J.*, *230*, 621, 1979.

Wu, C. S., C. S. Lin, H. K. Wong, S. T. Tsai, and R. L. Zhou, Absorption and emission of extraordinary-mode electromagnetic waves near cyclotron frequency in nonequilibrium plasmas, *Phys. Fluids*, *24*, 2191, 1981.

Yoon, P. H., and A. T. Weatherwax, A theory for AKR fine frequency structure, *Geophys. Res. Lett.*, *25*, 4461, 1998.

Zarka, P., Auroral radio emissions at the outer planets: Observations and theories, *J. Geophys. Res.*, *103*, 20,159, 1998.

Zarka, P., D. Le Quéau, and F. Genova, The maser synchrotron instability in an inhomogeneous medium: Determination of the spectral intensity of auroral kilometric radiation, *J. Geophys. Res.*, *91*, 13,542, 1986.

C. W. Carlson, Space Sciences Laboratory, University of California, Berkeley, CA 94720-7450, USA. (cwc@ssl.berkeley.edu)

R. E. Ergun, Department of Astrophysical and Planetary Sciences and Laboratory for Atmospheric and Space Physics, University of Colorado, Boulder, CO 80303, USA. (ree@fast.colorado.edu)

P. L. Pritchett, Department of Physics and Astronomy, University of California, 405 Hilgard Avenue, Los Angeles, CA 90095-1547, USA. (pritchet@physics.ucla.edu)

R. J. Strangeway, Institute of Geophysics and Planetary Physics, University of California, 405 Hilgard Avenue, Los Angeles, CA 90095-1567, USA. (strange@igpp.ucla.edu)

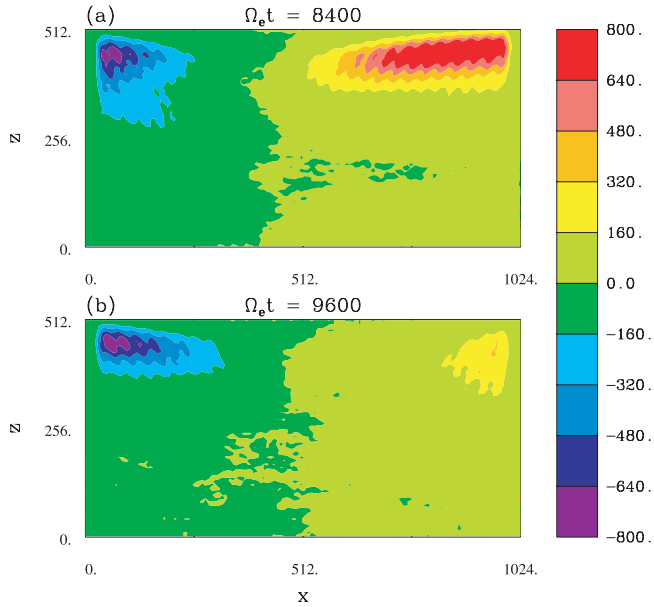

Figure 2. Contours of the x component of the Poynting vector at two different times (a) $\Omega_e t = 8400$ and (b) $\Omega_e t = 9600$ in a driven simulation with 5 keV shell electrons.

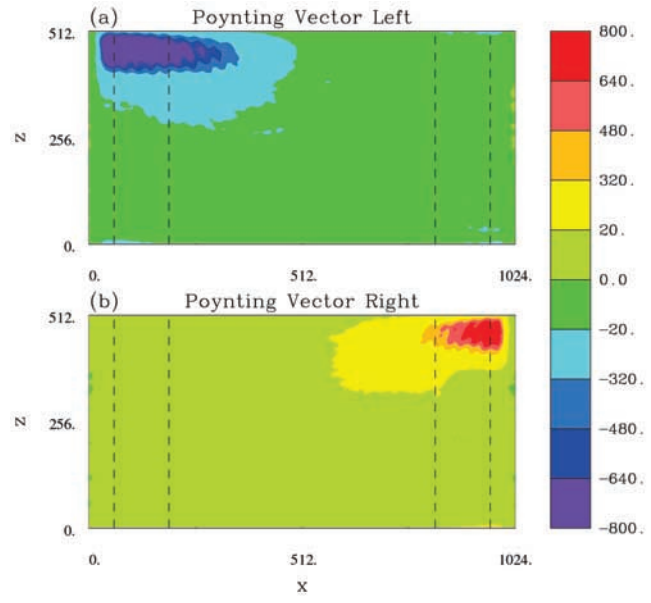

Figure 7. Contours of the x component of the Poynting vector decomposed into its (a) leftward and (b) rightward traveling components. The density of shell electrons within the two regions bounded by dashed vertical lines at the sides of the simulation domain is maintained at twice the value of the density in the central region.

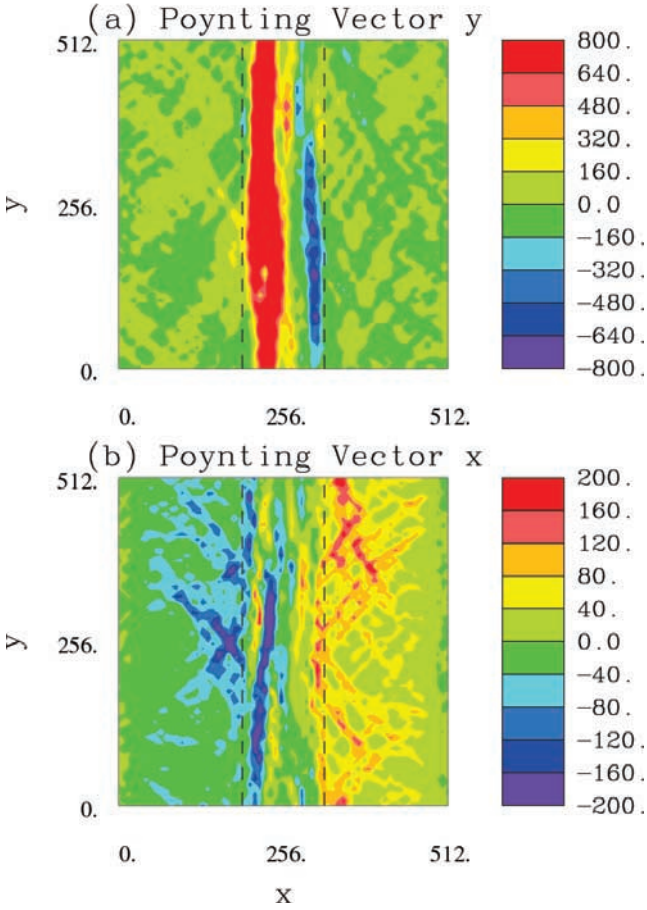

Figure 16. The (a) y and (b) x components of the Poynting vector at time $\Omega_e t = 1600$ for a narrow cavity simulation with 5 keV shell electrons.

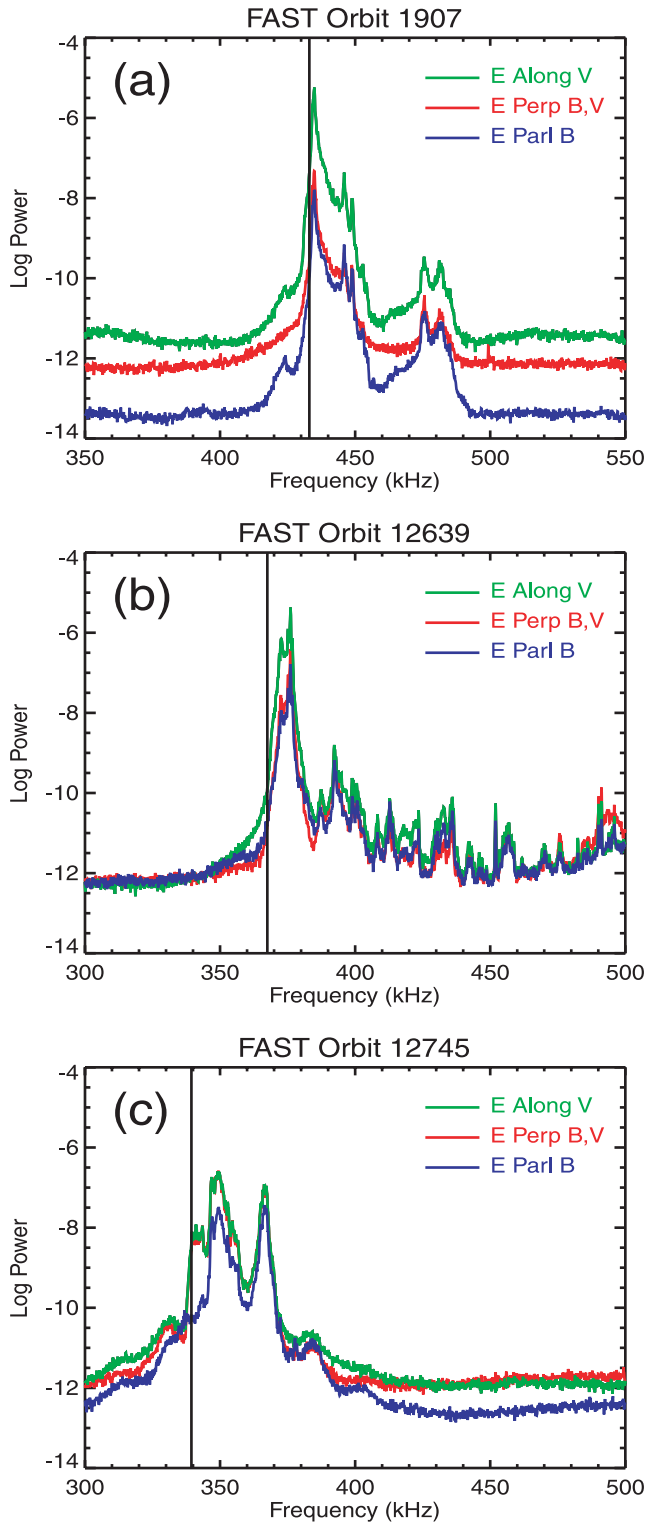

Figure 17. Power spectra for the three electric field components as determined from FAST crossings of the AKR source region on (a) orbit 1907 near 23 MLT, (b) orbit 12639 near 21 MLT, and (c) orbit 12745 near 21 MLT. The two perpendicular field components have been projected along directions parallel to the spacecraft trajectory and perpendicular to both B and the trajectory. In all panels the vertical solid line indicates the (nonrelativistic) electron cyclotron frequency.

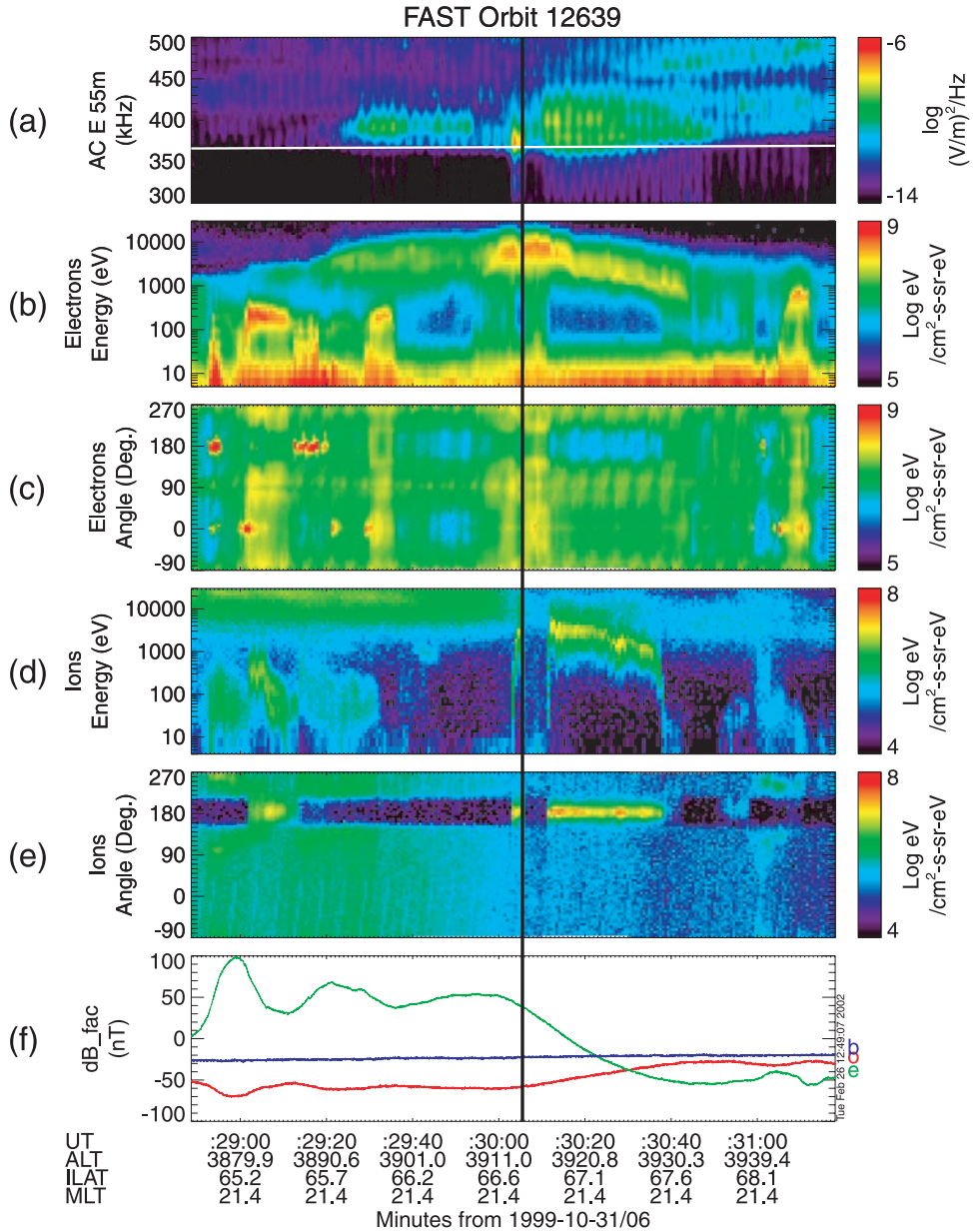

Figure 18. Particle and field data acquired by FAST on orbit 12639. (a) Electric field data in the frequency range 300–500 kHz. The white trace gives the local electron gyrofrequency. (b) Electron energy flux versus energy and time. (c) Electron energy flux versus pitch angle and time. (d) Ion energy flux versus energy and time. (e) Ion energy flux versus pitch angle and time. (f) The deviation of the observed magnetic field from the model field (IGRF 95) in field-aligned coordinates: outward (o), eastward (e), and model-field aligned (b). The vertical black line indicates the interval of HSBM data.

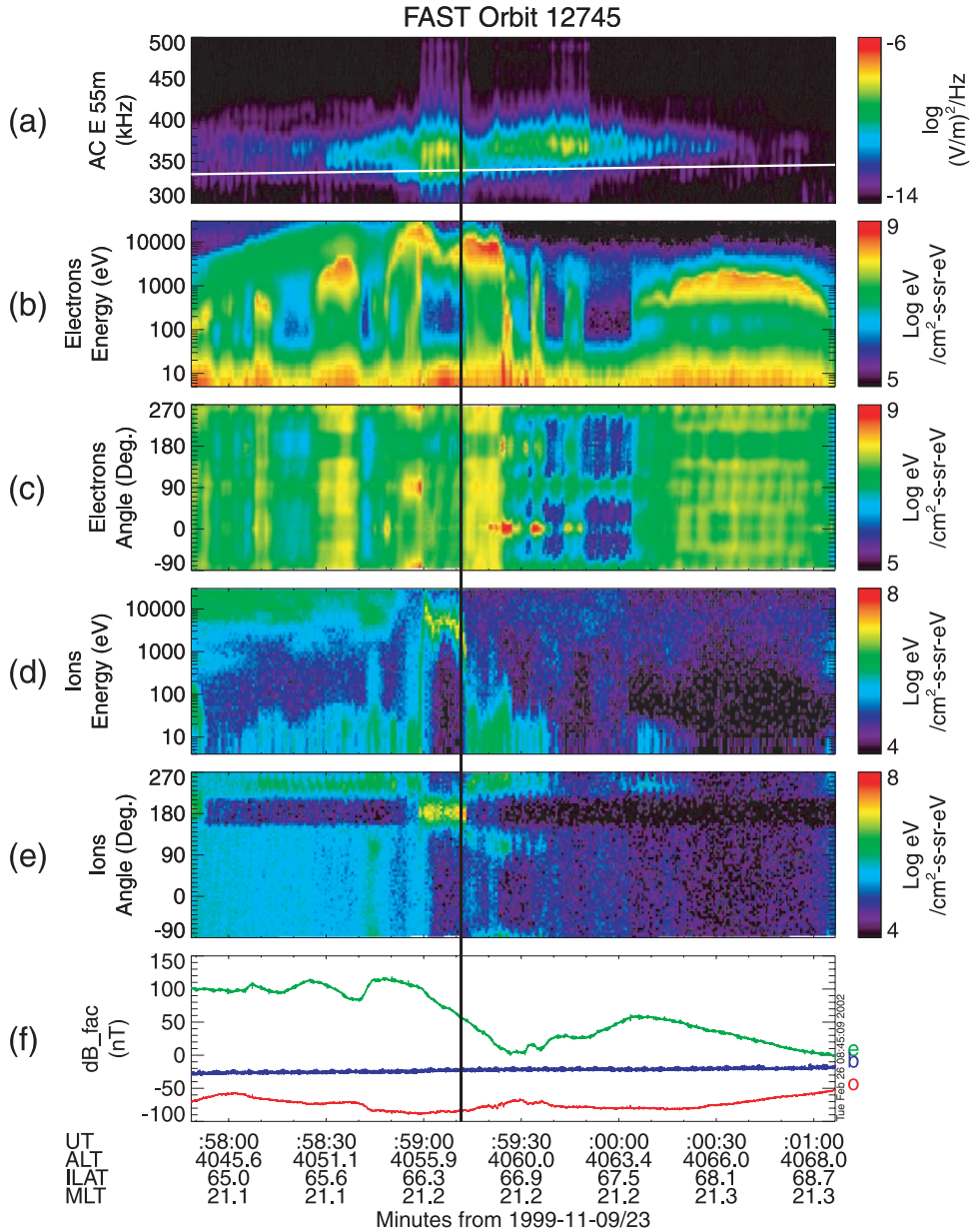

Figure 19. Same as Figure 18 but for orbit 12745.